RSC Advances

ROYAL SOCIETY OF CHEMISTRY

PAPER

View Article Online
View Journal | View Issue

Cite this: *RSC Adv.*, 2026, **16**, 26669

First-principles investigation of direct band gap double perovskite halides $A_2AgIrCl_6$ (A = Cs, Rb, K) for enhanced photovoltaic performance

M. A. Rayhan, *[abc] M. M. Hossain, [ab] M. M. Uddin[ab] and M. A. Ali *[ab]

This study carefully investigates the structural, electrical, optical, mechanical, and thermodynamic features of $A_2AgIrCl_6$ compounds (A = Cs, Rb, K) that belong to double perovskite halides (DPH) utilizing density functional theory (DFT). The stability of the predicted compounds in the cubic structure was confirmed through calculations involving the Goldschmidt tolerance factor, octahedral factor, and the new tolerance factor. Analysis of formation enthalpy, binding energy, phonon dispersion relations, and *ab initio* molecular dynamics (AIMD) results suggests thermodynamic and dynamic stability, indicating possible synthetic viability that should be verified experimentally. To predict the accurate optoelectronic properties, we employed the Tran and Blaha modified Becke-Johnson (TB-mBJ) potential. The electronic band structure study demonstrated that the studied halides exhibit direct band gap semiconductor with band gap values of 1.43 eV, 1.50 eV, and 1.55 eV for $Cs_2AgIrCl_6$, $Rb_2AgIrCl_6$, and $K_2AgIrCl_6$, respectively. The relatively low electron effective masses suggest favorable carrier transport characteristics. In addition, the calculated exciton binding energies and exciton radii indicate a tendency toward efficient generation of free charge carriers. The optical investigation further demonstrated that the $A_2AgIrCl_6$ compounds exhibit low reflectivity and high absorption coefficients (on the order of 10^5 cm^{-1}) in the visible region, highlighting their potential for optoelectronic applications. The computed elastic constants fulfill the Born–Huang criteria, confirming mechanical stability, while further analysis indicates ductile and anisotropic behavior. Overall, the calculated results suggest that the $A_2AgIrCl_6$ compounds exhibit promising optoelectronic descriptors favorable for further experimental and device-oriented evaluation.

Received 9th April 2026
Accepted 11th May 2026

DOI: 10.1039/d6ra02981g

rsc.li/rsc-advances

1 Introduction

The limited energy supplies of the Earth are put under stress by the increasing energy consumption caused by population expansion and growing living standards.[1,2] Over the previous 150 years, a notable increase in energy use has outpaced population growth. Fossil fuels, mainly gas and oil, account for over 80% of global use, which has issues with supply and impact on the environment. This clarifies how urgently renewable energy sources like geothermal, wind, and solar power need to be used.[3–5] Conservation and the use of renewable energy are becoming increasingly important to both governments and citizens. Of the possible substitutes, metal halide perovskites have garnered substantial interest and have been thoroughly studied in the past several years.[6] These materials have drawn much attention over the past ten years due to their unique characteristics, adaptable synthesis methods, and configurable device designs. Perovskites based on lead have become a viable and affordable alternative for high-efficiency solar cells. Meanwhile, their commercialization has been hampered by problems with lead toxicity and chemical instability despite their excellent efficiency.[7–9] Even though a number of lead-free perovskites have been suggested as a solution to the toxicity issue, they still have difficulty reaching comparable levels of efficiency.

Trivalent cations like Bi^{3+} and Sb^{3+} have recently been used to create 2D layered lead-free halide perovskites.[10] Researchers have also incorporated trivalent cations like Bi^{3+} together with monovalent cations such as Ag^{1+} into the B-sites of halide perovskites, resulting in the formation of B-cation double perovskites, which follow the general formula $A_2B'B''X_6$. Among these, $Cs_2AgBiBr_6$ and $Cs_2AgBiCl_6$ have emerged as compounds with promising photovoltaic properties and notable stability.[11–13] The experimentally determined optical band gap for $Cs_2AgBiCl_6$ and $Cs_2AgBiBr_6$ range from 2.20 eV to 2.77 eV and 1.83 eV to 2.19 eV, respectively.[12–14] In comparison,

[a]*Department of Physics, Chittagong University of Engineering and Technology (CUET), Chattogram-4349, Bangladesh. E-mail: rayhan4302@gmail.com; ashrafphy31@cuet.ac.bd*

[b]*Advanced Computational Materials Research Laboratory (ACMRL), Department of Physics, Chittagong University of Engineering and Technology (CUET), Chattogram-4349, Bangladesh*

[c]*Department of Arts & Sciences, Bangladesh Army University of Science and Technology (BAUST), Saidpur Cantonment, Saidpur-5310, Nilphamari, Bangladesh*

calculations using density functional theory (DFT) and hybrid functionals yield slightly higher band gap values, between 2.62 eV and 3.00 eV for $Cs_2AgBiCl_6$ and 2.06 eV to 2.30 eV for $Cs_2AgBiBr_6$.[12,14] Despite possessing band gap that lie within the visible spectrum, these materials display an indirect band gap nature, which restricts their usefulness for application in thin-film photovoltaic applications. Recent DFT studies have shown that modifying the B-site cations in DPH is an effective strategy for controlling their band gap and improving properties relevant to photovoltaic performance. In particular, recent work[15] on Ag- and Au-containing double perovskites demonstrated that deliberate changes in composition can significantly influence the electronic structure and light absorption behavior, thereby offering valuable understanding of how compositional design governs material properties in these systems. The fabrication of lead-free double perovskite halides with direct band gap has received substantial interest for its potential in optoelectronic and solar applications. Zhang *et al.*[16] proposed that integrating In^{1+} or Tl^{1+} with Bi^{3+} could result in direct band gap, a concept further reinforced by Zhao *et al.*,[17] who reported a direct band gap of 0.91 eV for $Cs_2InBiCl_6$. However, compounds like Cs_2InBiX_6 phase stability limits due to the oxidation of In^{1+} to In^{3+}.[18] In a separate study, S. Mahmud *et al.* conducted a theoretical analysis of the A_2AuScX_6 compounds, finding a band gap range of 1.30 to 1.93 eV, underlining its possibilities for usage in optoelectronic and photovoltaic systems.[19] Transition metals have also been introduced into DPH due to their unique electronic properties, leading to the synthesis and study of various compounds such as Cs_2AgCrX_6,[20,21] $Cs_2AgFeCl_6$,[22] and Cs_2NaVCl_6.[23] Single crystals of $Cs_2Ag_xNa_{1-x}FeCl_6$ and $Cs_2NaSc_{1-x}Cl_6 : xTb^{3+}$, have shown promise in photovoltaic and volumetric display technologies.[24–26] Additionally, transition metals from group VIII, including Co, Rh, and Ir, which are commonly found in oxide perovskites, are being studied for their potential in DPHs due to their distinctive optoelectronic properties, which are beneficial for applications in photovoltaic.[27–30] Recent research has renewed interest in Co, Rh, and Ir-based DPHs, with investigations of compounds like Rb_2NaCoF_6,[31] Cs_2AgRhX_6,[32,33] and Cs_2CuIrF_6.[34] Furthermore, a number of recent investigations have utilized integrated first-principles methodologies that simultaneously examine structural, electronic, optical, mechanical, and thermodynamic characteristics to assess the potential of double perovskites in optoelectronic applications.[35] These studies offer a unified computational approach for evaluating diverse material properties and serve as an important reference point for the current work. Despite these advances, many lead-free double perovskites still suffer from either indirect band gap or excessively wide band gap (>2.2 eV), limiting their photovoltaic performance.[14,36] More recently, V. Deswal *et al.* revealed that the DPH combination $Cs_2AgInBr_6$ had a direct band gap of 1.57 eV and a high predicted power conversion efficiency, highlighting its promise as appropriate B-site cation combinations.[37] A density functional theory investigation by Parves *et al.* (2025)[38] explored the DPH $X_2NaIrCl_6$ (X = Rb, Cs) to evaluate their prospects for optoelectronic and photovoltaic uses. The calculated electronic band structures reveal direct band gap of roughly 1.93 eV for $Cs_2NaIrCl_6$ and 2.02 eV for $Rb_2NaIrCl_6$, which lie within a suitable range for solar energy harvesting. In addition, these materials exhibit strong optical absorption, supporting their potential applicability in solar cell devices. Closely related compounds such as M_2KIrCl_6 (M = Cs, Rb)[39] have also been examined through first-principles calculations to understand their electronic and optical behavior for photovoltaic applications. The predicted direct band gap is about 1.99 eV for Cs_2KIrCl_6 and 2.10 eV for Rb_2KIrCl_6, suggesting that these materials are capable of efficiently utilizing visible light from the solar spectrum. Furthermore, recent reports have emphasized the importance of correlating optical and mechanical properties with compositional design in double perovskites, demonstrating how subtle changes in cation selection can influence structural stability and optoelectronic response.[40] These findings emphasize the necessity of systematic investigations to identify compositions that simultaneously satisfy stability and performance criteria.

Despite recent progress in Ir-based DPH such as $Cs_2NaIrCl_6$ and Cs_2KIrCl_6, these systems typically exhibit direct but relatively wide band gap (~1.9–2.1 eV), which are not optimal for photovoltaic applications. Therefore, identifying alternative B-site cation combinations that can simultaneously preserve direct band gap while reducing their magnitude remains a critical challenge. However, achieving direct band gap within the optimal photovoltaic range (~1.12–1.77 eV) remains a major unresolved challenge in lead-free DPHs.

In this work, we introduce a distinct compositional strategy by incorporating Ag^+ alongside Ir^{3+} in $A_2AgIrCl_6$ (A = Cs, Rb, K) compounds. Unlike previously studied Ir-based systems, the Ag/Ir combination enables strong Ag–Cl–Ir orbital hybridization, which significantly modifies the electronic structure. As a result, the studied compounds exhibit direct band gap in the range of 1.43–1.55 eV, placing them much closer to the optimal range for solar energy conversion.

To the best of our knowledge, Ag–Ir-based double perovskites remain largely unexplored. Therefore, this study presents a comprehensive first-principles investigation of $A_2AgIrCl_6$ compounds using the FP-LAPW technique based on the DFT framework, implemented *via* the Wien2k software package, covering their structural stability, electronic, optical, mechanical, and thermodynamic properties. This work thus represents a clear step beyond existing Ir-based double perovskites. The computational models and techniques used are described in Section 2, and the outcomes and their consequences are covered in Section 3. Section 4 provides an overview of our study's results.

2 Computational methods

This work investigated the structural, dynamical, mechanical, thermophysical, electrical, and optical properties of the $A_2AgIrCl_6$ compounds (A = Cs, Rb, K) using first-principles calculations. The calculations were conducted using DFT framework[41,42] with the FP-LAPW approach, as implemented in the Wien2k software package.[43,44] The exchange-correlation potential for the bulk structure of the double perovskite was

implemented utilizing the Perdew–Burke–Ernzerhof (PBE) formulation within the generalized gradient approximation (GGA).[45] Birch–Murnaghan's equation of state[46] was used to evaluate the structural parameters. The plane-wave cut-off value $R_{MT} \times k_{max}$, was set to 8.0, where R_{MT} refers to the radius of the smallest atomic muffin-tin sphere, and K_{max} indicates the maximum wave vector in the plane-wave basis set. Within the muffin-tin sphere, the maximum partial wave expansion was defined by $l_{max} = 10$. The muffin-tin radii were set to 2.50 a.u. (A), 2.13 a.u. (Ag), 2.18 a.u. (Ir), and 1.88 a.u. (Cl), with a Fourier expansion cutoff of $G_{max} = 14$ $(Ry^{1/2})$. A dense 1000 k-point mesh was used for Brillouin-zone sampling, and a core-valence separation energy of 7.0 Ry with a self-consistent convergence criterion of 10^{-5} Ry ensured numerical accuracy. The TB-mBJ potential was employed to obtain reliable optoelectronic band gap.[47] To ensure precise band gap measurement, the spin–orbit coupling (SOC) approach (TB-mBJ + SOC) was implemented. The crystal structure was visualized using VESTA.[48] Dynamic stability was assessed through phonon calculations using the CASTEP (Cambridge Serial Total Energy Package) package, employing a 2 × 2 × 2 supercell and finite-displacement method to obtain phonon dispersion and thermodynamic properties.[49]

3 Results and discussion

3.1 Structural parameters and stability

The $A_2AgIrCl_6$ compounds (A = Cs, Rb, K), shown in Fig. 1, crystallize in a face-centered cubic structure belonging to the $Fm\bar{3}m$ (No. 225) space group.[50] This structure consists of fourteen [$IrCl_6$] octahedra, thirteen [$AgCl_6$] octahedra, and eight A-site atoms (A = Cs, Rb, K) positioned within the interstitial spaces of the octahedra, which help maintain crystal stability.[51] Within this particular space group, the crystal structure of $A_2AgIrCl_6$ compounds places the A^{+1} cations in the 8c Wyckoff location with fractional coordinates (0.25, 0.25, 0.25). Ag^{+1} cations are located at the 4a Wyckoff site with coordinates (0.5, 0.5, 0.5), Ir^{+3} cations are at the 4b site at (0.0, 0.0, 0.0), and Cl^{-1} anions occupy the 24e Wyckoff site at (0.25, 0.0, 0.0). The

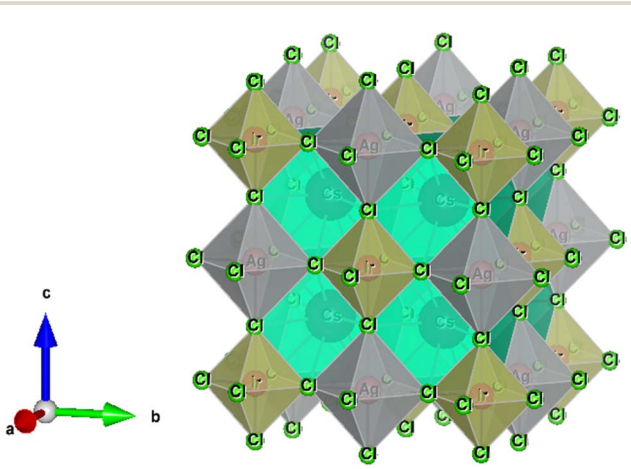

Fig. 1 The unit cell of $Cs_2AgIrCl_6$.

$A_2AgIrCl_6$ compounds have undergone optimization using volume optimization, as illustrated in Fig. 2. Table 1 presents the results of the geometry optimization-especially, the unit cell parameter a_0, bulk modulus B_0, its pressure derivative, and the ground state energy E_0. The selection of A-site cation significantly influences the lattice constant of the conventional cell, which reduces sequentially from Cs to Rb to K. There are currently no experimental results available for direct comparison with these findings in the scientific literature.

To comprehensively assess the stability of the $A_2AgIrCl_6$ compounds, it is necessary to perform calculations for both their dynamic stability, represented by phonon dispersion calculations and their thermodynamic stability. However, since these calculations are computationally demanding and time-consuming, we initially evaluate the stability of the compounds by computing parameters such as final energy, decomposition enthalpy, formation energy, binding energy, Goldschmidt tolerance factor, octahedral factor, and a new tolerance factor. The final energy values per atom for $Cs_2AgIrCl_6$, $Rb_2AgIrCl_6$, and $K_2AgIrCl_6$ were determined to be −2149.64 eV, −2004.61 eV, and −2023.32 eV, respectively.

To evaluate the thermodynamic stability of $A_2AgIrCl_6$ compounds, we compute their decomposition energy along different potential pathways. The primary and most significant pathway involves the decomposition of $A_2AgIrCl_6$ compounds into the respective binary materials. Halide perovskites are generally synthesized *via* the reverse reactions of their constituent binary materials. Specifically, we determine the decomposition energy, which is defined as follows:

$$\Delta H_D = 2E[ACl] + E[AgCl] + E[IrCl_3] - E[A_2AgIrCl_6] \quad (1)$$

where, E[ACl], E[AgCl], E[$IrCl_3$] and E[$A_2AgIrCl_6$] are the final energies of ACl, AgCl, $IrCl_3$ and $A_2AgIrCl_6$, respectively.[52] The computed ΔH_D values are given in Table 1. These values indicate that all $A_2AgIrCl_6$ compounds are thermodynamically stable, as reflected by their positive values. However, a clear trend is observed among the compound: $K_2AgIrCl_6$ exhibits a comparatively lower decomposition energy than $Cs_2AgIrCl_6$ and $Rb_2AgIrCl_6$, suggesting reduced thermodynamic stability and a higher tendency toward decomposition under practical conditions. Moreover, to assess the thermodynamical stability of the perovskite materials, formation energy (E_f) and binding energy (E_B) are calculated through the formula mentioned:[53]

$$E_f = \frac{E_{A_2AgIrCl_6} - n_A \times E_A - n_{Ag} \times E_{Ag} - n_{Ir} \times E_{Ir} - n_{Cl} \times E_{Cl}}{40} \quad (2)$$

$$E_B = \frac{E_{A_2AgIrCl_6} - n_A \times \mu_A - n_{Ag} \times \mu_{Ag} - n_{Ir} \times \mu_{Ir} - n_{Cl} \times \mu_{Cl}}{40} \quad (3)$$

In this context, $E_{A_2AgIrCl_6}$ signifies the overall energy of DPH compounds, whereas E_A, E_{Ag}, E_{Ir} and E_{Cl} represent the energies of individual A (A = Cs, Rb, K), Ag, Ir, and Cl atoms, correspondingly. The variable 'n' denotes the number of atoms and 'μ' symbolizes the free energy of each atom. The computed

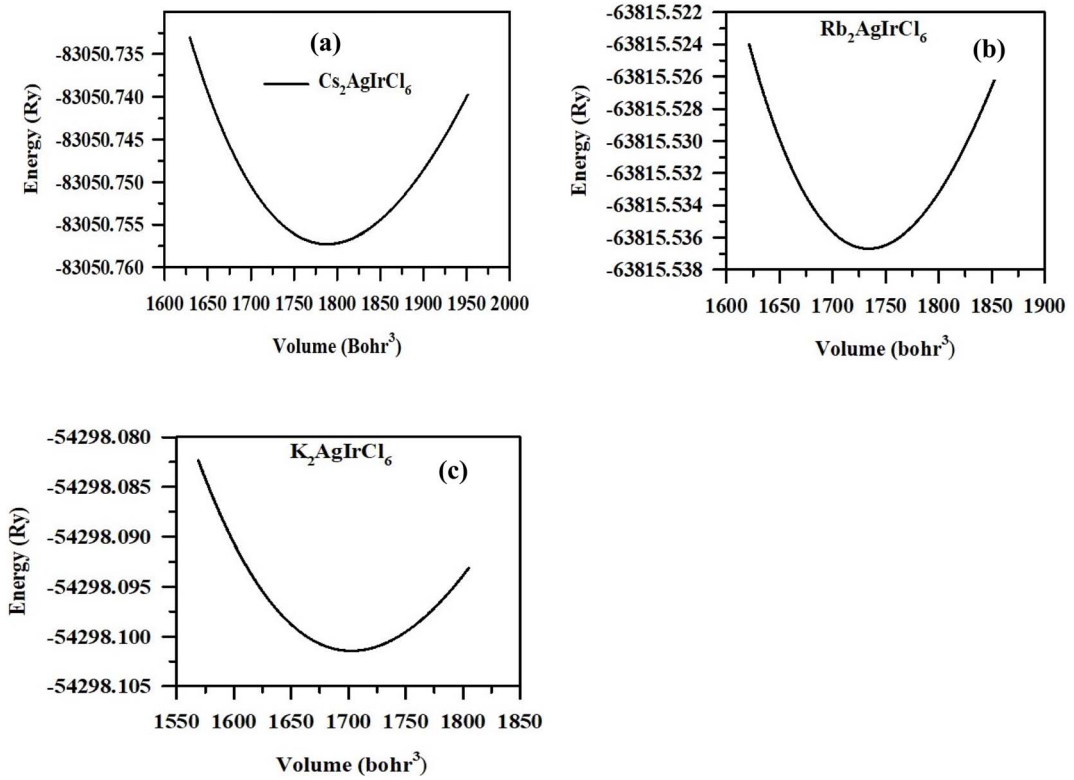

Fig. 2 (a–c) The optimized energy *versus* volume plots fitted using the Birch–Murnaghan equation for $A_2AgIrCl_6$ compounds where A = Cs, Rb, K.

Table 1 Calculated values of lattice parameter a_0, bulk modulus B_0, it's derivative $B_0^{'}$, total energy E_{tot}, decomposition energy ΔH_D, formation energy E_f and binding energy E_B for $A_2AgIrCl_6$ compounds A = Cs, Rb, K

DPH	a_0 (Å)	B_0 (GPa)	$B_0^{'}$	E_{tot} (Ry)	ΔH_D (meV/atom)	E_f (eV/atom)	E_B (eV/atom)
$Cs_2AgIrCl_6$	10.19	41.53	5.32	−83050.76	73.55	−2.10	−4.29
$Rb_2AgIrCl_6$	10.09	44.03	5.60	−63815.54	50.66	−2.06	−4.28
$K_2AgIrCl_6$	10.03	44.93	5.47	−54298.10	0.19	−2.03	−4.28

formation energies (E_f) and binding energies (E_B) for $A_2AgIrCl_6$ compounds are presented in Table 1. These values exhibit negativity, indicating that these three compounds should be synthesizable, and they comply with thermodynamical stability criteria. Of the three compounds, the E_f and E_B values indicate that $K_2AgIrCl_6$ compound is thermodynamically the least stable, in agreement with the decomposition energy analysis.

The crystallographic stability of perovskite structures is frequently determined using the Goldschmidt tolerance factor '*t*' (as specified in eqn (4))[54] and the octahedral factor '*u*' (as defined in eqn (5)),[55] both of which serve as trustworthy indications for predicting structural stability. 'τ', a new tolerance factor newly introduced by Bartel and co-workers to eqn (6),[56] has demonstrated a high level of prediction accuracy. The parameters *t*, *u*, and τ are calculated as follows:

$$t = \frac{(R_A + R_X)}{\sqrt{2}(R_B + R_X)} \quad (4)$$

$$u = \frac{R_B}{R_X} \quad (5)$$

$$\tau = \frac{R_X}{R_B} - n_A\left(n_A - \frac{R_A/R_B}{\ln(R_A/R_B)}\right) \quad (6)$$

In these equations, n_A is the oxidation state of A, with $R_A > R_B$ by definition. R_A, R_B, and R_X are the ionic radii of A, B, and X ions, respectively in an ABX_3 structure. R_B is calculated as the average ionic radius of Ag^+ and Ir^{3+} for double perovskites. A stable perovskites requires *t* between 0.81 – 1.11, *u* between 0.41 – 0.90, and $\tau \leq 4.18$.[54–56] These values were determined using Shannon's ionic radii[57] and are listed in Table 2. Although all compounds lie within the acceptable stability range for perovskite structures, $K_2AgIrCl_6$ lies closer to the lower stability limit and suggesting reduced structural stability compared to the Cs- and Rb-based systems. This observation is consistent with decomposition energy, formation energy and binding energy analysis. This suggests that while $K_2AgIrCl_6$ remains a viable

Table 2 Shannon's ionic radii (r), Goldschmidt tolerance factor (t), octahedral factor (u), and new tolerance factor (τ) for $A_2AgIrCl_6$ compounds A = Cs, Rb, K

DPH	Ionic radius of cations (Å)		Ionic radius of Cl ion (Å)	Tolerance factor (t)	Octahedral factor (u)	New tolerance factor (τ)
$Cs_2AgIrCl_6$	r_{Cs} 1.88	$(r_{Ag} + r_{Ir})/2$ 0.92	r_{Cl} 1.81	0.96	0.51	3.83
$Rb_2AgIrCl_6$	r_{Rb} 1.72	$(r_{Ag} + r_{Ir})/2$ 0.92	r_{Cl} 1.81	0.91	0.51	3.93
$K_2AgIrCl_6$	r_{K} 1.64	$(r_{Ag} + r_{Ir})/2$ 0.92	r_{Cl} 1.81	0.89	0.51	4.04

candidate, its experimental synthesis and long-term stability may require more careful consideration.

3.2 Phonon stability and AIMD simulations

Fig. 3 displays the phonon dispersion curves (PDCs) and phonon density of states (PDOS) for $A_2AgIrCl_6$ compounds (A = Cs, Rb, K). A dynamics matrix, derived from force constants, illustrates the variation in force experienced by a standard atom due to the orientation of neighboring atoms. The matrices' diagonals are then isolated, representing eigen-values and eigenvectors, indicative of fundamental phonon frequencies and motion. The results show three acoustic and several optical phonon modes, consistent with the phonon dispersion curves. However, upon deploying conventional unit cells, it was found that two modes were degenerate, underscoring the importance of cell structure in determining degeneracy accurately.[33]

The conventional unit cell of $A_2AgIrCl_6$ compounds comprises forty atoms, resulting in a variety of acoustic and optical phonon modes. Among these, three acoustic modes at the Γ point are characterized by low frequencies ranging from 0 to 1.25 THz, while the remaining optical modes fall within the high-frequency range of 1.25 to 10 THz. Fig. 3 indicates the absence of soft phonon modes in the material, as all phonon modes exhibit positive lattice vibration frequencies. This indicates that the material is dynamically stable within the present computational framework. The phonon stability of $A_2AgIrCl_6$ compounds is maintained along the pathways W to L, L to Γ, Γ to X, X to W, and W to K, suggests stability across the entire pathway. The PDOS of the compound is presented alongside the dispersion curve. It is shown that lattice vibrations at low frequencies, less than 1.0 THz, correspond to optical modes and are primarily impacted by A-site atoms, namely Cs, Rb, and K. On the other hand, the low and mid-frequency vibrations are mostly controlled by Ag, Ir, and Cl atoms. Higher frequencies primarily affect the vibrational behavior due to the interaction between Ir and Cl ions.

To further assess thermal behavior, AIMD simulations were performed using a 2 × 2 × 2 supercell at 300 K for 10 000 fs within the NVE ensemble.[58] The variation of total energy with simulation time is illustrated in Fig. 4. For $Cs_2AgIrCl_6$ shown in Fig. 4a, the total energy oscillates between −149.93 eV and −146.53 eV, giving an average value of −148.56 eV. The corresponding deviations from the mean energy are approximately 0.92% and 1.36%, indicating only minor thermal perturbations. In the case of $Rb_2AgIrCl_6$ represented in Fig. 4b, the energy values fall within a slightly narrower interval ranging from −149.97 eV to −147.85 eV, with an average of −148.83 eV. The deviations from the mean are relatively small (0.76% and 0.66%), suggesting stable dynamical behavior throughout the simulation period. Similarly, for $K_2AgIrCl_6$ depicted in Fig. 4c, the total energy varies from −149.59 eV to −147.29 eV, producing an average energy of −148.95 eV, with deviations of 0.42% and 1.11% from the mean value.

The absence of sudden energy jumps during the entire simulation interval indicates that the crystal frameworks remain preserved at room temperature. Such steady and bounded energy oscillations are characteristic of dynamically stable structures under finite-temperature conditions. Similar stability characteristics have previously been observed in other halide perovskite systems, such as $A_2AlAgBr_6$ (A = K, Rb, Cs)[59] and $CuMCl_3$ (M = Ge, Sn).[60] We have also extended our AIMD calculations to 30 000 fs at 300 K and 500 K, as shown in Fig. S1 (supplementary part), to further examine the finite-temperature structural stability of the investigated compounds within the simulation timescale. These observations provide additional computational evidence supporting the finite-temperature stability of the $A_2AgIrCl_6$ compounds within the limits of the present theoretical approach and may be relevant for future experimental and optoelectronic investigations.

3.3 Electronic properties

The features of direct band gap semiconductors make them more favorable for optical applications than those with indirect band gap.[61] The GGA-calculated band gap (E_g) for $Cs_2AgIrCl_6$ is 0.34 eV, suggesting the potential for electron transitions between the valence band maximum (VBM) and the conduction band minimum (CBM). Substituting lighter alkali atoms (A = Cs, Rb, K) at the A-site in $A_2AgIrCl_6$ compounds has a minimal impact on E_g, with values ranging from 0.34 to 0.38 (see Table 3). In contrast, the TB-mBJ functionals yield much higher E_g values of 1.43 eV for $Cs_2AgIrCl_6$, 1.50 eV for $Rb_2AgIrCl_6$, and 1.55 eV for $K_2AgIrCl_6$ (see Table 3), respectively. This mismatch shows that compared to the TB-mBJ functional, GGA functionals tend to significantly underestimate E_g while maintaining the direct nature of band gap between VBM and CBM. The GGA functional underestimates the band gap,[62–64] while the TB-mBJ functional provides results that closely match the experimental values documented in the literature.[65–67] Both approximations consistently yield a direct band gap nature at the same high symmetry points. The calculated band gap of $A_2AgIrCl_6$ compounds exhibit a systematic increase when moving from Cs to Rb to K at the A-site, independent of the exchange–correlation functional used. This trend originates primarily from structural and electronic effects induced by A-site cation

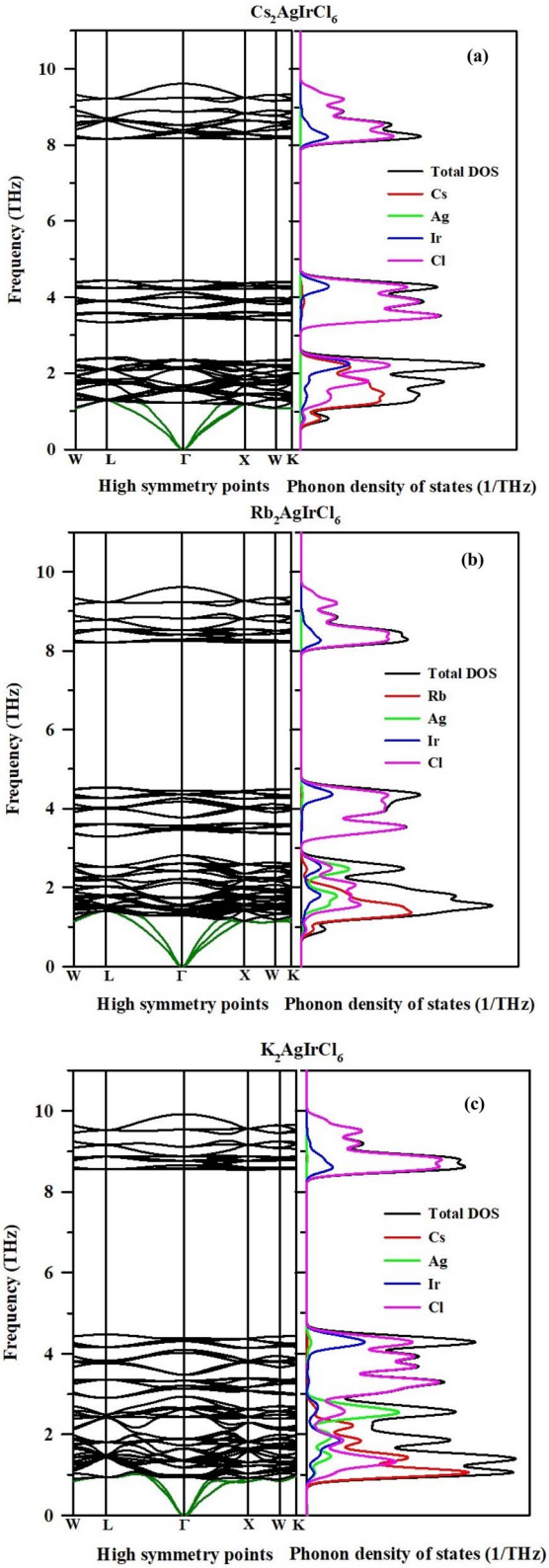

Fig. 3 (a–c)The phonon dispersion spectra and corresponding phonon DOS for $A_2AgIrCl_6$ compounds where A = Cs, Rb, K.

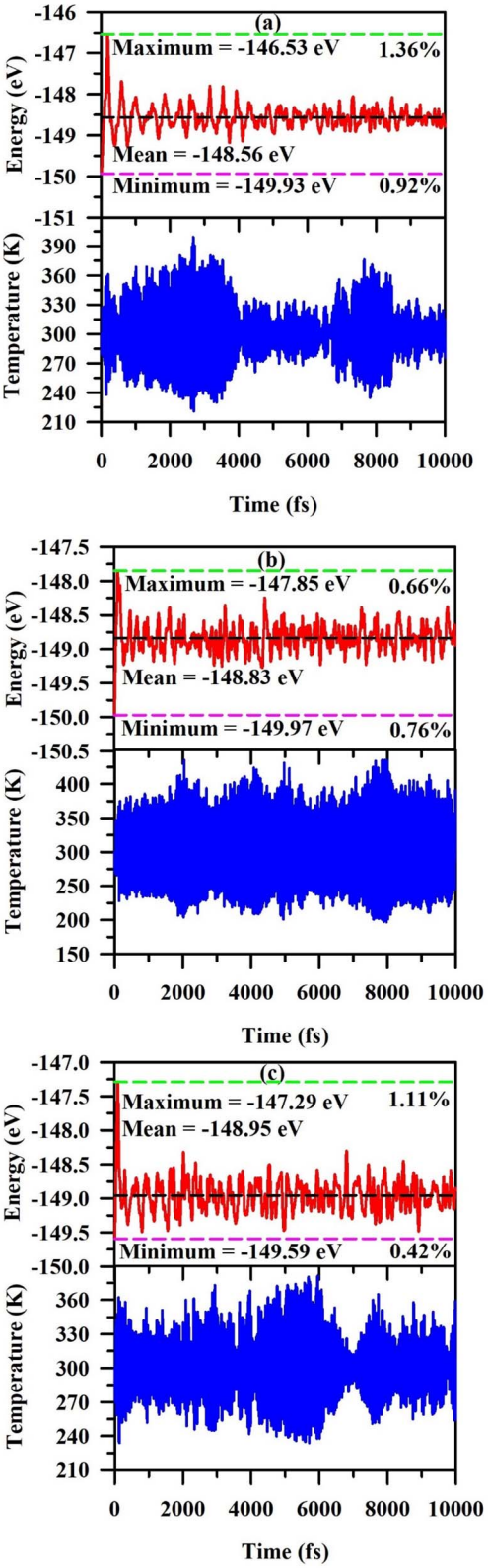

Fig. 4 The variation in energy profiles and temperature as a function of time step (fs) for (a) $Cs_2AgIrCl_6$, (b) $Rb_2AgIrCl_6$, and (c) $K_2AgIrCl_6$.

substitution, rather than direct electronic participation of the alkali metal states near the band edges. As the ionic radius of the A-site cation decreases ($Cs^+ \rightarrow Rb^+ \rightarrow K^+$), the lattice constant correspondingly contracts, leading to shorter Ag–Cl and Ir–Cl bond lengths and enhanced octahedral tilting. This structural contraction strengthens the orbital overlap between

Table 3 Calculated band gap by different approaches, band gap nature, and calculated electron and hole effective mass values, reduced effective masses, exciton binding energy in meV and exciton radius in nm of the $A_2AgIrCl_6$ compounds where A = Cs, Rb, K

DPH	Band gap (eV)	Functional	Band gap nature	Effective mass of electron, m_e^*	Effective mass of hole, m_h^*	Reduced effective mass, μ_r^*	Static dielectric constant (ε_s)	Exciton binding energy (E_b)	Exciton radius (a_0^*)	Ref.
$Cs_2AgIrCl_6$	0.34	GGA PBE	Direct	0.13 m_e	1.10 m_e	—	—	—	—	This
	1.43	TB-mBJ	Direct	0.19 m_e	1.43 m_e	0.168 m_e	4.41	117.53	1.39	
	1.42	TB-mBJ + SOC	Direct	—	—	—	—	—	—	
$Rb_2AgIrCl_6$	0.36	GGA PBE	Direct	0.13 m_e	1.10 m_e	—	—	—	—	This
	1.50	TB-mBJ	Direct	0.18 m_e	1.70 m_e	0.163 m_e	4.27	121.63	1.39	
	1.53	TB-mBJ + SOC	Direct	—	—	—	—	—	—	
$K_2AgIrCl_6$	0.38	GGA PBE	Direct	0.13 m_e	1.64 m_e	—	—	—	—	This
	1.55	TB-mBJ	Direct	0.18 m_e	1.14 m_e	0.155 m_e	4.20	119.50	1.43	
	1.60	TB-mBJ + SOC	Direct	—	—	—	—	—	—	
$Cs_2NaIrCl_6$	0.92	GGA PBE	Direct	0.21 m_e	1.33 m_e	—	—	—	—	38
	1.93	TB-mBJ	Direct	0.30 m_e	1.69 m_e	—	—	—	—	
$Rb_2NaIrCl_6$	0.97	GGA-PBE	Direct	0.20 m_e	1.10 m_e	—	—	—	—	38
	2.02	TB-mBJ	Direct	0.29 m_e	1.41 m_e	—	—	—	—	
Cs_2KIrCl_6	1.08	GGA-PBE	Direct	0.23 m_e	1.51 m_e	—	—	—	—	39
	1.99	TB-mBJ	Direct	0.32 m_e	1.98 m_e	—	—	—	—	
Rb_2KIrCl_6	1.12	GGA-PBE	Direct	0.23 m_e	1.24 m_e	—	—	—	—	39
	2.10	TB-mBJ	Direct	0.32 m_e	1.63 m_e	—	—	—	—	
$Cs_2AgInCl_6$	3.02	HSE	Direct	0.272 m_e	0.520 m_e	0.178 m_e	2.760	319	0.819	78
Cs_2AgIrF_6	1.07	GGA PBE	Indirect	0.46 m_e	3.64 m_e	—	—	—	—	79
	1.65	TB-mBJ	Indirect	0.29 m_e	0.99 m_e	—	—	—	—	
Rb_2AgIrF_6	1.13	GGA PBE	Indirect	0.47 m_e	4.98 m_e	—	—	—	—	79
	1.76	TB-mBJ	Indirect	0.28 m_e	0.94 m_e	—	—	—	—	
K_2AgIrF_6	1.16	GGA PBE	Indirect	0.38 m_e	6.20 m_e	—	—	—	—	79
	1.83	TB-mBJ	Indirect	0.27 m_e	0.84 m_e	—	—	—	—	

Ir-5d and Cl-3p states, which predominantly define both the VBM and CBM. The increased crystal field splitting and modified p–d hybridization results in a widening of the band gap.

Fig. 5 illustrates band structure computations for $A_2AgIrCl_6$ compounds using GGA-PBE (left) and TB-mBJ (right), revealing a significant behavioral similarity. Our discussion exclusively focuses on TB-mBJ for its superior accuracy in energy band gap values over GGA. To further evaluate relativistic effects, spin–orbit coupling (SOC) was included in the TB-mBJ calculations. Although Ir is a heavy element with strong intrinsic relativistic effects, a significant SOC influence might be expected. However, the calculated results show that SOC introduces only relatively minor changes in the electronic structure, mainly in the form of band splitting near high-symmetry points, while the overall band dispersion and band gap remain largely unchanged. This seemingly modest SOC effect can be understood from the nature of the band edge states. Even though Ir 5d orbitals are intrinsically sensitive to SOC, the valence and conduction band edges are not solely governed by Ir states. Instead, they originate from significant hybridization between Ir 5d and Cl 3p orbitals. This hybridization effectively spreads the electronic character over different atomic species, which in turn lessens the direct influence of SOC on the band edge positions. Consequently, SOC primarily perturbs the fine structure of the bands rather than inducing substantial shifts in the band gap. Similar behavior has been reported in related double perovskite systems, where orbital mixing mitigates the expected strong SOC influence of heavy elements.[19,68] Perovskite materials with band gap values between 0.8 and 2.2 eV[69] are highly fit for a comprehensive range of photovoltaic applications, particularly in photovoltaic conversion processes. The $A_2AgIrCl_6$ compounds, with their band gap falling within this ideal range, carry significant potential for development as photosensitive materials for future solar cell technologies. Their band gap properties make them promising candidates used for improving the efficiency then effectiveness of photovoltaic conversion in solar energy applications.

Analyzing the density of states (DOS) and electronic band structure plots for the $A_2AgIrCl_6$ compounds (see Fig. 5 and 6), our investigation reveals that the VBM predominantly comprises the character of Cl(3P) and Ir(5d). Specifically, the valence band dispersion immediately under the Fermi level is significantly influenced by the Ir 5d and the Cl 3p orbitals. In the case of $Cs_2AgIrCl_6$, the calculated normalized contribution to the VBM is 65.2% for Ir(5d) and 20.6% for Cl(3p). Similarly, for $Rb_2AgIrCl_6$ (and $K_2AgIrCl_6$), the contributions to the VBM for Ir(5d) and Cl(3p) are 65.0 (64.5)% and 19.2 (17.9)%, respectively. Interestingly, the alkali and Ag atoms demonstrate minimal contributions, hovering around 1–2%, to the VBM for $A_2AgIrCl_6$ compounds. Conversely, our examination of the CBM reveals a predominant derivation from Ir(5d) empty anti-bonding states with significant contributions from Ag, Ir, and Cl states, causing its dispersion well above the Fermi level. The normalized contributions to the CBM for $A_2AgIrCl_6$ compounds are (57.2, 57.1, 56.8)% for Ir(5d), (27.1, 27.0, 26.8)% for Cl(3p), and (5.8, 5.8, 6.0)% for Ag(4d), respectively. Notably, these contributions exhibit marginal variations upon the substitution of the A-site

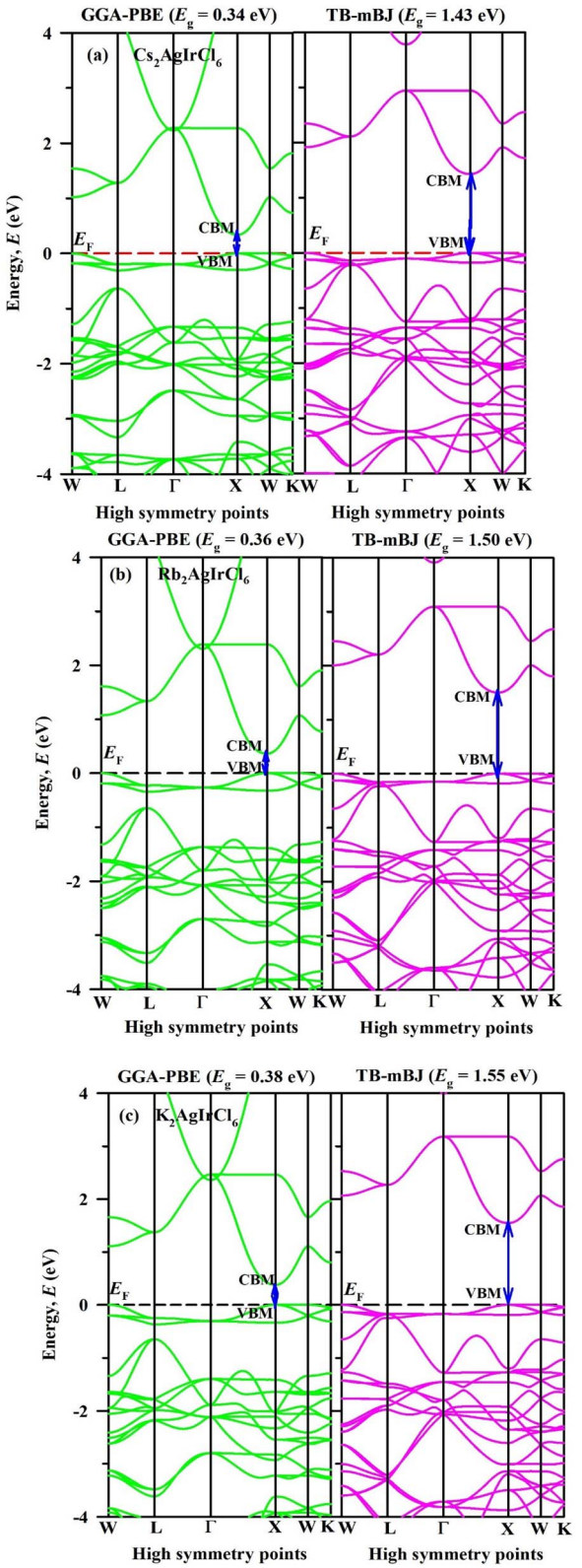

Fig. 5 Band structure of (a) $Cs_2AgIrCl_6$, (b) $Rb_2AgIrCl_6$, and (c) $K_2AgIrCl_6$ compounds using GGA-PBE (left panel, green color) and TB-mBJ (right panel, pink color) functionals.

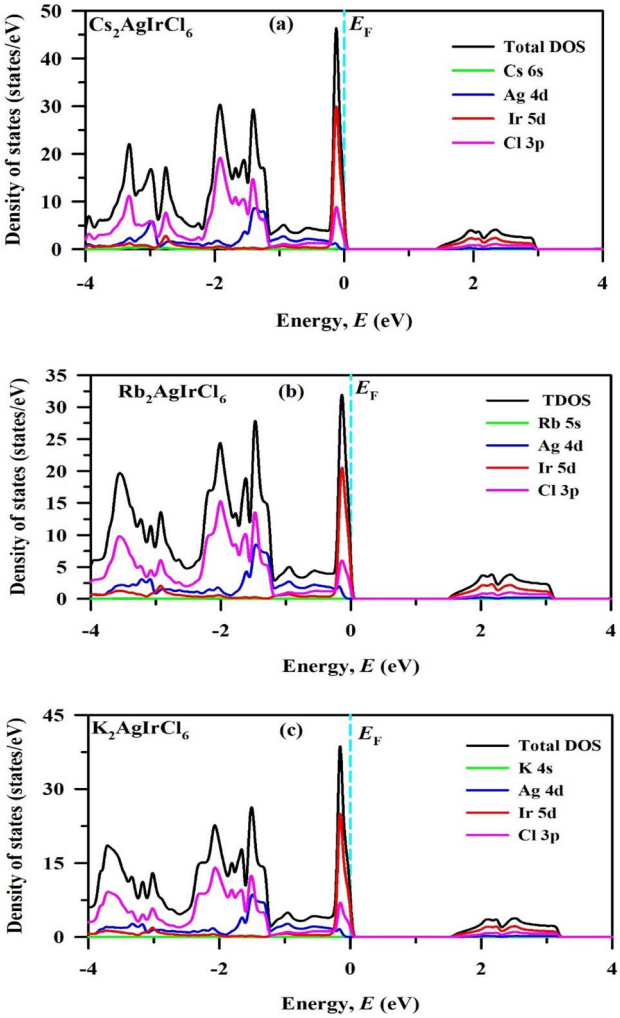

Fig. 6 Density of states of (a) $Cs_2AgIrCl_6$, (b) $Rb_2AgIrCl_6$, and (c) $K_2AgIrCl_6$ compounds.

cation with lighter alkali group elements. Considering the substantial separation between the CBM and VBM, coupled with the VBM's proximity to the Fermi level, these results suggest a valence-band structure dominated by Ir–Cl states, which may favor hole participation in transport.[70] Very large DOS peaks just below the Fermi level come from the nearly localized Ir(5d) electrons. The electronic properties of $A_2AgIrCl_6$ DPHs are governed by strong Ir–Cl–Ag hybridization, which controls band gap and reduces effective SOC impact at band edges.

Understanding the photovoltaic properties of solar cells depends on study on the effective masses of electrons and holes as it directly influences carrier mobility, resistivity, and the optical response of free charge carriers.[71] We observed that the VBM is less dispersed compared to the CBM. A comparable flat valence band feature has been observed in bulk $Cs_2AgInCl_6$, mainly due to the hybridization of Ag 4d and Cl 3p orbitals.[72] In such cases, it's common for the hole effective mass (m_h^*) linked with the VBM to be greater than the electron effective mass (m_e^*) of the CBM. Consequently, the hole mobility is less than electron mobility. This is because, the band curvature is inversely related to the second derivative of energy concerning the wave vector k and is elucidated by the dispersion relationship:[73]

$$m^* = \pm \frac{\hbar^2}{\left(\mathrm{d}^2E(k)/\mathrm{d}k^2\right)} \quad (7)$$

In this context, the symbols "+" and "–" represent electrons and holes, respectively. Here, m^* refers to the effective mass of either the electron or hole, k stands for the wave vector, $E(k)$ denotes the energy as a function of k, and $\hbar$ represents the reduced Planck constant. The second derivative of energy regarding the wave vector, $\mathrm{d}^2E(k)/\mathrm{d}k^2$, is obtained by fitting a parabolic function to the E–k dispersion at the symmetry points. The estimated effective masses of electrons and holes for the investigated compounds are summarized in Table 3. For $Cs_2AgIrCl_6$, the electron's effective mass is approximately 0.19 m_e and the hole's is 1.43 m_e, with m_e being the free electron mass. For $Rb_2AgIrCl_6$, these values are 0.18 m_e and 1.70 m_e, respectively; and for $K_2AgIrCl_6$, they are 0.18 m_e and 1.14 m_e. All these values were computed using the TB-mBJ functionals. It is found that while the effective masses of holes are larger than the free electron mass (m_e), the effective masses of electrons are all smaller. The fact that the hole effective masses (m_h^*) in Table 3 are significantly greater than the electron effective masses (m_e^*) indicates a pronounced asymmetry between electron and hole effective masses, which may influence carrier transport behavior.[74] Additionally, while effective mass and mobility are inversely related, Table 3 shows that both charge carriers have very modest effective masses, indicating increased carrier mobility.[75] With promising performance across a wide variety of solar applications, our findings demonstrate the great potential of $A_2AgIrCl_6$ compounds for usage in photovoltaic technology.

The exciton binding energy E_b plays a critical role in solar cell materials. For efficient charge separation, this energy needs to be low. A low E_b means that thermal energy at room temperature can easily separate bound electron–hole pairs (excitons) into free charge carriers. In contrast, a high exciton binding energy keeps electrons and holes paired, reducing carrier mobility, and increasing recombination losses, which negatively impact the solar cell's performance. Excitonic behavior arises from the Coulomb attraction between photo-generated electrons and holes. We have calculated E_b for the $A_2AgIrCl_6$ compounds using the Wannier–Mott exciton model with the static dielectric constant by the following relation:[76]

$$E_b = \frac{\mu_r^*}{m_e}\frac{R}{\varepsilon_s^2} \quad (8)$$

$$a_0^* = \varepsilon_s \frac{m_e}{\mu_r^*} a_0 \quad (9)$$

where,

$$\mu_r^* = \frac{m_e^* m_h^*}{m_e^* + m_h^*} \quad (10)$$

where, R = 13.6057 eV is the Rydberg energy constant, a_0 = 0.5292 Å is the Bohr radius constant, ε_s is the static dielectronic

constant, m_e is the mass of free electron and μ_r^* is the reduced effective mass of the electron–hole pair. Table 3 lists the resulting excitonic parameters. For $Cs_2AgIrCl_6$, $Rb_2AgIrCl_6$, and $K_2AgIrCl_6$, we have found exciton binding energies of approximately 117.53 meV, 121.63 meV, and 119.50 meV, and corresponding exciton radii on the order of 1.39 nm, 1.39 nm, and 1.43 nm. These exciton binding energies are somewhat smaller and exciton radii larger when compared with the previous similar studies.[77,78] The comparatively low exciton binding energy and larger exciton radius indicate a weaker electron–hole Coulomb interaction, so that excitons dissociate quickly into free electrons and holes, which is favorable for the solar cell applications. Therefore, the $A_2AgIrCl_6$ compounds are promising candidates for photovoltaic applications due to their low exciton binding energies and rapid generation of free charge carriers.

3.4 Charge density

To better understand the electronic behavior of the investigated compounds, the cross-sectional charge density distribution of $A_2AgIrCl_6$ compounds within the (110) crystallographic plane was computed and is shown in Fig. 7. The charge density was calculated using the TB-mBJ approach based on a fully converged wavefunction.[80,81] From the contour plots, one can observe a mixed bonding character consisting of partial ionic and covalent interactions within the crystal. A pronounced charge accumulation is observed along the Ir–Cl bonds, which suggests significant covalent interaction between Ir and Cl atoms. This behavior may be attributed to the hybridization between Ir-5d and Cl-3p orbitals and is consistent with the PDOS results. In contrast, the Ag–Cl bonds exhibit relatively weaker and more symmetric charge distribution, suggesting moderate covalent character with a partial ionic contribution arising from Ag-4d and Cl-3p hybridization. Furthermore, no significant charge overlap is observed directly between Ag and Ir atoms, indicating the absence of direct bonding and suggesting that their interaction is mediated through Cl atoms. On the other hand, the absence of substantial charge accumulation in the regions between the A-site cations ($Cs^+/Rb^+/K^+$) and Cl^- ions, along with the nearly spherical charge distribution around the A-site atoms, is consistent with predominantly ionic A–Cl interactions. Therefore, the bonding in $A_2AgIrCl_6$ compounds can be qualitatively described as a combination of relatively strong Ir–Cl covalent interactions, weaker Ag–Cl hybridization, and predominantly ionic A–Cl interactions, which collectively govern the electronic structure of the $A_2AgIrCl_6$ compounds. Across the series from Cs to K, the overall charge distribution pattern remains similar, although a slight increase in charge overlap is observed with decreasing lattice size, which may be associated with enhanced orbital interaction. Similar qualitative trends have been reported in earlier studies.[19,79,82,83] It should be noted that the present bonding interpretation is

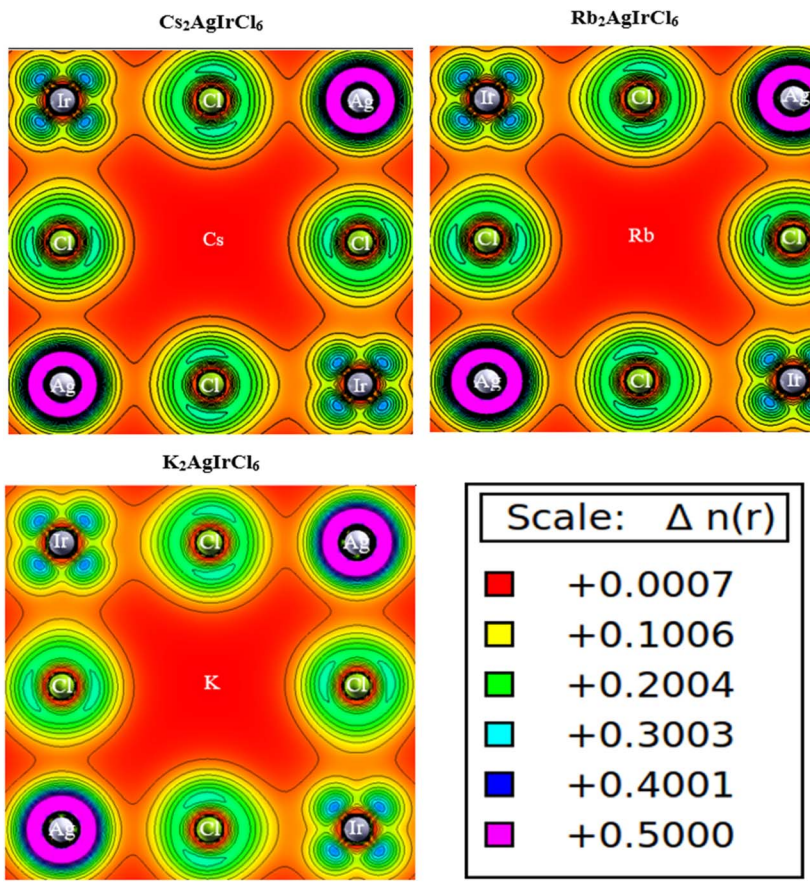

Fig. 7 Charge density of $A_2AgIrCl_6$ compounds where A = Cs, Rb, K.

qualitative in nature and that more quantitative bonding characterization would require additional analyses such as Bader charge analysis, electron localization function (ELF), crystal orbital Hamilton population (COHP), or related approaches.

3.5 Optical properties

The optical response of $A_2AgIrCl_6$ compounds was analyzed to understand light-matter interactions and their relation to the electronic structure. The calculated direct band gaps (1.43–1.55 eV) suggest that these compounds are suitable for visible-light absorption. The frequency dependent complex dielectric function encapsulates the complete material response to electromagnetic radiation-induced perturbations,[84] expressed by the equation $\varepsilon(\omega) = \varepsilon_1(\omega) + i\varepsilon_2(\omega)$.[85] The real part of dielectric constant $\varepsilon_1(\omega)$ describes the dispersive response of the material, while the imaginary part of dielectric constant $\varepsilon_2(\omega)$ represents interband electronic transitions. In Fig. 8a and b, we compared the spectra of $\varepsilon_1(\omega)$and $\varepsilon_2(\omega)$ for $A_2AgIrCl_6$ compounds within the energy range of 0 eV to 14 eV. The static dielectric function $\varepsilon_1(0)$ assumes values of 4.41, 4.27, and 4.20 for $Cs_2AgIrCl_6$, $Rb_2AgIrCl_6$, and $K_2AgIrCl_6$, respectively, mirroring those of $Cs_2AgRhCl_6$ (A = Li, K, Na, Rb, Cs),[33] Cs_2XRhCl_6 (X = Na, K),[86] and $Cs_2AgBiCl_6$.[87] As the A-site cation changes from Cs^+ to Rb^+ to K^+, the ionic radius decreases, leading to a gradual contraction of the lattice and enhanced distortion of the [$AgCl_6$] and [$IrCl_6$] octahedra. This structural contraction reduces the electronic polarizability of the lattice, which directly results in a decrease in the static dielectric constant $\varepsilon_1(0)$ from $Cs_2AgIrCl_6$ to $K_2AgIrCl_6$. Substitution of heavier alkali metals results in a higher value. Additionally, $\varepsilon_1(\omega)$ rises with ascending photon energy for each perovskite material, reaching maximum values of 10.84, 10.76, and 10.55 at energies 2.24 eV, 2.33 eV, and 2.38 eV for $Cs_2AgIrCl_6$, $Rb_2AgIrCl_6$, and $K_2AgIrCl_6$, respectively. Following this, there is a rapid decline in $\varepsilon_1(\omega)$ characterized by oscillations and multiple peaks. In certain intervals, $\varepsilon_1(\omega)$ records values below zero, indicating an impediment for photons with corresponding energies to penetrate the solid materials. Penn's model delineates an inverse correlation between static polarization and the band gap, articulated as:[88]

$$\varepsilon_1(0) \approx 1 + \left[\frac{\hbar\omega_p}{E_g}\right]^2 \quad (11)$$

In this expression, $\hbar$ denotes the reduced Planck constant, and ω_p refers to the plasma frequency.

The significance of $\varepsilon_2(\omega)$lies in its pivotal role in determining the peak optical absorption and monitoring interband electronic transitions within materials. Due to inherent limitations in DFT, there are slight deviations in the electronic transition points between the valence and conduction bands, as evidenced in Fig. 8b. The maximum value of $\varepsilon_2(\omega)$, often referred to as the first absorption peak (FAP), is indicative of significant electronic transitions near the Fermi energy. In the $A_2AgIrCl_6$ compounds, the FAP appears at photon energies of approximately 2.38 eV, 2.46 eV, and 2.52 eV, respectively, highlighting minor variations in electronic structure influenced by the choice of A-site cation.

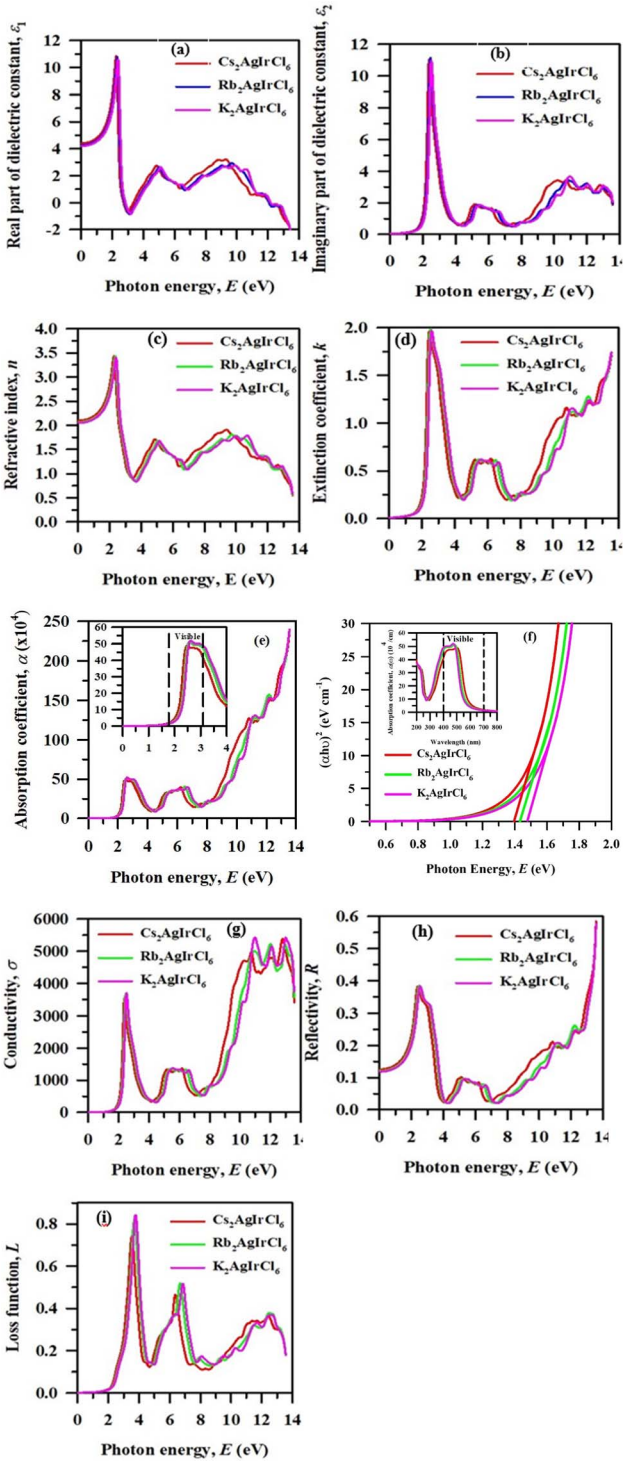

Fig. 8 (a–i) Optical properties of $A_2AgIrCl_6$ compounds where A = Cs, Rb, K.

These are situated at energies higher than those observed in the $\varepsilon_1(\omega)$ curves (refer to the above). The primary focus for these compounds is on the highest FAP values. These values fall within the visible range, indicating an effective absorption capacity for visible light. In comparison to the DOS, the first absorption spectrum (FAS) primarily stems from the Ir-d and Cl-p orbitals at the VBM and the CBM points.

The refractive factor $n(\omega)$, extinction factor $k(\omega)$, absorption coefficient $\alpha(\omega)$, conductivity $\sigma(\omega)$, reflectivity $R(\omega)$, and loss factor $L(\omega)$, which are essential optical constants, are derived from the dielectric properties of all compounds using prescribed equations given below:[89,90]

$$n(\omega) = \left[\frac{\varepsilon_1(\omega)}{2} + \frac{\sqrt{\varepsilon_1^2(\omega) + \varepsilon_2^2(\omega)}}{2}\right]^{1/2} \quad (12)$$

$$k(\omega) = \left[\frac{-\varepsilon_1(\omega)}{2} + \frac{\sqrt{\varepsilon_1^2(\omega) + \varepsilon_2^2(\omega)}}{2}\right]^{1/2} \quad (13)$$

$$\alpha(\omega) = \frac{2\omega}{c}k(\omega) \quad (14)$$

$$\sigma(\omega) = \frac{4\varepsilon_0 E}{e}\varepsilon_2(\omega) \quad (15)$$

$$R(\omega) = \frac{(n-1)^2 + k^2}{(n+1)^2 + k^2} \quad (16)$$

$$L(\omega) = \frac{\varepsilon_2(\omega)}{\varepsilon_1^2(\omega) + \varepsilon_2^2(\omega)} \quad (17)$$

The complex refractive index ($n + ik$) is an essential characteristic of solid materials, offering information about how light travels through them and their possible use in optoelectronic technologies.[91] Using eqn (12) and (13), we determined the real components of the complex refractive index. The value of $n(\omega)$ varies depending on the material, while semiconductors typically have a small $k(\omega)$.[92] The outcomes of the refractive index calculation are presented in Fig. 8c. The real part of dielectric function shows a behavior akin to that of the refractive index since $n^2(\omega) = \varepsilon_1(\omega)$.[55] The static refractive index values for $A_2AgIrCl_6$ compounds at zero frequency are 2.09, 2.06, and 2.04, respectively. Consequently, the higher dielectric screening in $Cs_2AgIrCl_6$ leads to a larger refractive index, while reduced screening in $K_2AgIrCl_6$ yields a smaller $n(0)$. The peak values of $n(\omega)$ at energies of 2.27, 2.35, and 2.41 eV for $A_2AgIrCl_6$ compounds are 3.44, 3.43, and 3.40. The measured refractive indices fall within the typical range (2.5 to 3.5)[91] reported for DPHs, indicating consistent optical behavior. The extinction coefficient $k(\omega)$ exhibits a consistent resemblance to the patterns of $\varepsilon_2(\omega)$ and $\alpha(\omega)$, indicating the detection of electromagnetic wave loss in materials, as illustrated in Fig. 8d. The relationship between $k(\omega)$ and $\alpha(\omega)$ is as follows: $k = \frac{\alpha\lambda}{4\pi}$.

Device performance is strongly influenced by the material's light absorption capability.[93] The absorption coefficient, $\alpha(\omega)$, in semiconductors plays a crucial role in explaining how materials absorb photons and produce electron–hole pairs, which is fundamental to the functionality of photovoltaic devices like solar cells. In the present case, the absorption coefficient $\alpha(\omega)$ exhibits a pattern similar to that of $\varepsilon_2(\omega)$, as evidenced by their coefficients at different energies and wavelengths in Fig. 8e. For $A_2AgIrCl_6$ compounds, the absorption edge aligns well with the electronic band gap, confirming the direct-gap nature of these materials. The curve displays initial peaks at 2.46, 2.57, and 2.62 eV, respectively, all within the visible range. This emphasizes their suitability for visible-light-driven applications such as solar cells and photodetectors.[94] The appearance of many peaks within the higher energy range (6.0 to 13.5 eV), each with differing intensities, shows a diverse of transitions occurring between occupied and unoccupied electronic states. The first peak of the absorption coefficient ($\alpha_{max}(\omega)$) is observed approximately 4.9×10^5, 5.1×10^5, and 5.2×10^5 cm^{-1} at photon energies of 2.49, 2.57, and 2.62 eV for $Cs_2AgIrCl_6$, $Rb_2AgIrCl_6$, and $K_2AgIrCl_6$, respectively. The absorption coefficients of our investigated compounds surpass those of others, ranging from 6.12 to 6.58×10^4 cm^{-1} for A_2CuSbX_6 (A = Cs, Rb, K; X = Cl, Br, I),[95] 3 to 6.5×10^4 cm^{-1} for Cs_2CuBiX_6 (X = Cl, Br, I),[96] 2.3 to 3.4×10^5 cm^{-1} for Cs_2AgBiX_6 (X = Cl, Br, I).[97] They are consistent to those of Cs_2XRhCl_6 (ref. 86) and $Cs_2AgRhCl_6$ (ref. 33) (around 10^5), as observed in the highest peaks of DPH compounds within the visible range (400–700 nm). As shown in Fig. 8f, the absorption peaks for the $A_2AgIrCl_6$ compounds are observed at 498 nm, 482 nm, and 477 nm, respectively. These peaks all fall within the visible light spectrum of 380–780 nm, indicating that these DPH have strong absorption coefficients for visible light. The optical band gap in the studied DPH is determined through the established Tauc plot derived from absorption coefficient spectra.[98] Precisely determining the optical band gap is crucial for predicting semiconductor properties. However, improper application of the Tauc plot may lead to misinformation, especially in estimating the band gap.[99] The absorption behavior of a material can be analyzed using the Tauc equation, $(\alpha h\nu)^{1/\eta} = A(h\nu - E_g)$, where, α for absorption coefficient, h for Planck's constant, ν for photon frequency, A is a constant specific to the material, and E_g is the optical band gap energy.[98] The exponent η is determined by the nature of the band gap, generally set to 1/2 for direct band gap semiconductors and 2 for indirect ones. Based on the electronic band structure, $A_2AgIrCl_6$ compounds exhibits direct band gap; therefore, $\eta = 1/2$ was used in constructing the Tauc Plots. The linear fitting was performed in the near-edge region of the absorption spectra, where $(\alpha h\nu)^2$ shows approximately linear behavior, while avoiding both the low-energy tail and higher-energy non-linear regions. As shown in Fig. 8f, the estimated optical band gap for $A_2AgIrCl_6$ compounds is calculated as 1.40, 1.43, and 1.48 eV, respectively, using the TB-mBJ functional. These values are consistent with those obtained from the electronic structure calculations, reinforcing the reliability of the results.

Optical conductivity, described by eqn (15), governs electron conduction in materials when exposed to specific photon frequencies. Optoelectronic devices require the optical conductivity, linked to interband electron movement, to be between 1.4 eV and 4.0 eV in the visible spectrum.[36] Alkali metal substitution has minimal impact on conductivity. The primary conductivity peaks for $Cs_2AgIrCl_6$, $Rb_2AgIrCl_6$, and $K_2AgIrCl_6$ occur at 2.38 eV (3534 Ω^{-1} cm^{-1}), 2.46 eV (3691 Ω^{-1} cm^{-1}), and 2.51 eV (3699 Ω^{-1} cm^{-1}), respectively, with the highest peak

Table 4 Computed values of real part of dielectric constant $\varepsilon_1(0)$, refractive index $n(0)$, reflectivity $R(0)$, first peak of the absorption coefficient $\alpha_{max}(\omega)$, and optical band gap using Tauc plot for $A_2AgIrCl_6$ compounds where A = Cs, Rb, K

DPH	$\varepsilon_1(0)$	$n(0)$	$R(0)$	$\alpha_{max}(\omega) \times 10^5$ cm^{-1} at eV	Optical band gap (eV)	Ref.
$Cs_2AgIrCl_6$	4.41	2.10	0.125	4.90 at 2.49	1.40	This
$Rb_2AgIrCl_6$	4.27	2.07	0.121	5.10 at 2.57	1.43	This
$K_2AgIrCl_6$	4.20	2.05	0.118	5.20 at 2.62	1.48	This
Cs_2KIrCl_6	2.77	1.66	0.06	3.50 at 3.00	—	39
Rb_2KIrCl_6	2.68	1.64	0.06	3.80 at 3.20	—	39
$Cs_2NaIrCl_6$	2.78	1.67	0.06	3.90 at 4.00	—	38
$Rb_2NaIrCl_6$	2.65	1.63	0.06	3.50 at 4.20	—	38
Cs_2AgIrF_6	3.77	1.94	0.10	5.10 at 2.96	1.52	79
Rb_2AgIrF_6	3.52	1.88	0.09	5.40 at 3.00	1.61	79
K_2AgIrF_6	3.44	1.85	0.09	5.50 at 3.03	1.75	79
Cs_2AuYCl_6	2.44	1.55	0.11	0.23	—	82
Rb_2AuYCl_6	2.36	1.52	0.11	0.35	—	82

observed in the range of 5200 to 5500 Ω^{-1} cm^{-1} from 11 to 13 eV, as illustrated in Fig. 8g. These peaks, predominantly influenced by Ir-5d states, play a crucial role in the material's overall electronic structure. These findings affirm the high optical conductivity of these materials in the visible region.

The reflectance spectra of $A_2AgIrCl_6$ compounds are analyzed in Fig. 8h. Calculated static reflection coefficients $R(0)$ for $A_2AgIrCl_6$ compounds are 0.125, 0.121, and 0.118. Minimal reflectivity $R(\omega)$ suggests efficient light capture within the energy range from zero to the band gap. $R(0)$ increases with the substitution of heavier alkali atoms, and peak positions around 2.5 eV for $A_2AgIrCl_6$ compounds correspond to a maximum reflectance of about 38%. Fig. 8i displays the energy loss function, representing the electrons' energy loss as they move. Notable peaks at approximately 3.52 eV ($Cs_2AgIrCl_6$), 3.68 eV ($Rb_2AgIrCl_6$), and 3.76 eV ($K_2AgIrCl_6$) indicate electron dispersion around these energies, correlating with optical conductivity. Materials with low reflectivity and loss function values are valuable for potential use in solar cell absorbing layers. The computed values of real part of dielectric constant $\varepsilon_1(0)$, refractive index $n(0)$, reflectivity $R(0)$, first peak of the absorption coefficient $\alpha_{max}(\omega)$, and optical band gap using Tauc plot for $A_2AgIrCl_6$ compounds are given in Table 4. Overall, the calculated optical properties indicate that $A_2AgIrCl_6$ compounds exhibit favorable light absorption and electronic transitions for optoelectronic applications.

3.6 Mechanical properties

Though the study of opto-electronic properties of the titled compounds is our prime motivation, we have also studied the mechanical properties with the intention of checking the mechanical stability and their ductility (ductility is always desired for fabricating any devices), which is then further extended up to elastic moduli as a routine check. Studying important characteristics such bulk modulus, shear modulus, Young's modulus, Poisson's ratio, and Pugh's ratio help one to have a thorough knowledge of a material's mechanical performance. These characteristics offer vital information about the material's stiffness, brittleness or ductility, and toughness characteristics—all of which are crucial for determining if it is appropriate for a certain technical application. These properties collectively dictate how the material reacts to strain, significantly influencing its overall mechanical performance. The change in the A site from Cs to Rb to K in $A_2AgIrCl_6$ (A = Cs, Rb, K) compounds induces a shift in the lattice parameter, significantly impacting the material's elastic constants, as outlined in Table 5. It is imperative to assess mechanical stability before delving into the analysis of these characteristics. Typically, C_{ij} coefficients are used to provide the criteria for Born stability, which determines the mechanical stability of a lattice.[100,101] These coefficients play an important role in determining the structural integrity of a material under varied mechanical stresses. C_{11}, C_{12}, and C_{44} are the three particular elastic constants (C_{ij}) of the cubic double perovskite structure. Determining the lattice's mechanical stability requires knowledge of these constants. For a cubic crystal, Born stability conditions are $C_{11} - C_{12} > 0$, $C_{11} + 2C_{12} > 0$, and $C_{44} > 0$. These conditions correspond to the Born criterion, the spinodal criterion, and the shear criterion, respectively. More precisely, to guarantee the material's mechanical stability, the spinodal criteria, which is connected to the bulk modulus, needs to be positive.[102] Table 5 shows that $A_2AgIrCl_6$ compounds meets all Born, spinodal, and shear criteria, demonstrating mechanical

Table 5 Elastic constants C_{ij} (GPa), mechanical stability criteria, Cauchy pressure, and calculated mechanical parameters-bulk modulus (B), Shear modulus (G), Young modulus (Y), Poisson's ratio (ν), Pugh's ratio (B/G), and anisotropy coefficient A_Z-for $A_2AgIrCl_6$ compounds where A = Cs, Rb, K

Parameters		$Cs_2AgIrCl_6$	$Rb_2AgIrCl_6$	$K_2AgIrCl_6$
Born stability	C_{11} (GPa)	90.86	99.71	97.74
	C_{12} (GPa)	19.55	19.59	18.15
	C_{44} (GPa)	18.18	15.62	13.37
	C_{11}–C_{12} (GPa)	71.31	80.12	79.59
	$C_{11} + 2C_{12}$ (GPa)	129.96	138.89	134.04
Cauchy pressure, C_P (GPa)		1.37	3.97	4.78
Bulk modulus, B (GPa)		43.32	46.30	44.68
Shear modulus, G (GPa)		23.97	23.03	21.07
Young modulus, Y (GPa)		60.70	59.26	54.63
Poisson's ratio, ν		0.27	0.29	0.30
Pugh's ratio, B/G		1.81	2.01	2.12
Zener anisotropy index, A_Z		0.51	0.39	0.34

stability. Compared to other considered perovskites, the $Rb_2AgIrCl_6$ double perovskite exhibits the highest elastic C_{ij} value. By using the Cauchy pressure, which is $C'' = C_{12} - C_{44}$, one can determine if a material is brittle or ductile. A negative C'' value indicates brittleness, whereas a positive number indicates ductile behavior. All of the compounds under investigation have positive Cauchy pressure values, as shown in Table 5, which validates their ductile nature. Of them, $K_2AgIrCl_6$ has the highest C'' value, indicating that it is the most ductile, while $Cs_2AgIrCl_6$ has the lowest, showing that it is somewhat less ductile. Additionally, a distinct pattern is seen in the $A_2AgIrCl_6$ compounds, where the Cauchy pressure falls as the A-site cation's ionic radius increases. This inverse association suggests that the compound's decreased ductility is a result of higher A-site cations.

The Shear modulus (G), Bulk modulus (B), B/G, Young modulus (Y), and Poisson's ratio (ν) are calculated based on elastic constants using the Voigt–Reuss–Hill approximation[103] (refer to Table 5). The values assigned to Y, namely 60.70, 59.26, and 54.63 GPa for $Cs_2AgIrCl_6$, $Rb_2AgIrCl_6$, and $K_2AgIrCl_6$, respectively, serve as indicators of the respective materials' rigidity. Notably, the higher Y value for $Cs_2AgIrCl_6$ implies a greater stiffness when compared to $Rb_2AgIrCl_6$, and $K_2AgIrCl_6$. The observation that $Rb_2AgIrCl_6$ exhibits a larger B value than other two compounds further reinforce its superior resistance to deformation. Moving on to brittleness and ductility classification *via* the parameter ν, the Poisson's ratio with a threshold value of 0.26,[104] $Cs_2AgIrCl_6$, $Rb_2AgIrCl_6$, and $K_2AgIrCl_6$ are categorized as ductile materials with ν values of 0.27, 0.29, and 0.30, respectively. The B/G ratio, another crucial factor indicative of ductility or brittleness,[105] supports the notion of ductility for $Cs_2AgIrCl_6$, $Rb_2AgIrCl_6$, and $K_2AgIrCl_6$, with computed values of 1.81, 2.01, and 2.12, respectively. These values align with the calculated ν values, collectively suggesting a susceptibility to heat shocks. The positive Cauchy pressure values, specifically 1.37 for $Cs_2AgIrCl_6$, 3.97 for $Rb_2AgIrCl_6$, and 4.78 GPa for $K_2AgIrCl_6$, further confirm the ductile nature of the studied compounds, providing additional validation for their resistance to external stresses. An important metric for material characterization is the Zener anisotropy index (A_Z), determined by the relation $A_Z = 2C_{44}/(C_{11} - C_{12})$.[106] The resulting A_Z values of 0.51 for $Cs_2AgIrCl_6$, 0.39 for $Rb_2AgIrCl_6$, and 0.34 for $K_2AgIrCl_6$ unequivocally classify all the studied materials as anisotropic in nature. This aligns with findings from other perovskite materials, such as Cs_2CuIrF_6,[34] A_2CuSbX_6 (A = Cs, Rb, K; X = Cl, Br, I),[95] Cs_2AgBiX_6 (X = Cl, Br, I)[97] which were identified as mechanically stable, hard, incompressible, and anisotropic.

Additionally, the corresponding anisotropic elastic parameters for each phase may be used to determine the characteristics of homogeneous isotropic and anisotropic polycrystals, such as B, G, Y, and ν (see Table 6). The ELATE software is utilized to calculate these attributes.[107] Additional proof of anisotropic characteristics can be seen in the 3D contour plots for $A_2AgIrCl_6$ compounds in Fig. 9. Anisotropy is shown in Y when A is greater than one, meaning that none of the materials under study are spherical. A symmetric spherical shape exhibiting isotropy in linear compressibility (β) is generated when $A = 1$. Based on the β values, it appears that the materials being studied behave in an isotropic manner. Moreover, anisotropy is shown in the ranges of maximum and least deformation for G and ν under applied stresses. $Cs_2AgIrCl_6$ < $Rb_2AgIrCl_6$ < $K_2AgIrCl_6$ is the order of anisotropy in elastic moduli.

3.7 Thermal properties

One important thermodynamic parameter that is necessary to comprehend the characteristics and heat capacity of solids at various temperatures is the Debye temperature (θ_D). It provides information on how material properties change as a result of temperature changes. To compute θ_D, a number of theoretical models have been established; these models usually use formulas that take into account the average sound velocity (v_m).[108] This parameter plays a crucial role in studying and predicting the thermal behavior and stability of materials.

$$\theta_D = \frac{\hbar}{k_B}\left[\frac{3n}{4\pi V}\right]^{\frac{1}{3}} \times v_m \quad (18)$$

Table 6 Minimal and maximal values of elastic modulus and elastic anisotropy of $A_2AgIrCl_6$ compounds where A = Cs, Rb, K

	Young's modulus (GPa)		Linear compressibility (TPa^{-1})		Shear modulus (GPa)		Poisson's ratio	
DPH	Y_{min}	Y_{max}	β_{min}	β_{max}	G_{min}	G_{max}	ν_{min}	ν_{max}
$Cs_2AgIrCl_6$	47.85	83.94	7.69	7.69	18.18	35.65	0.11	0.47
$Rb_2AgIrCl_6$	41.86	84.81	7.64	7.64	15.62	36.06	0.10	0.53
$K_2AgIrCl_6$	36.47	92.05	7.46	7.46	13.37	39.79	0.07	0.61
Elastic anisotropy A_x								
	A_Y		A_β		A_G		A_ν	
$Cs_2AgIrCl_6$	1.75		1.00		1.96		4.19	
$Rb_2AgIrCl_6$	2.03		1.00		2.31		5.37	
$K_2AgIrCl_6$	2.52		1.00		2.98		8.30	

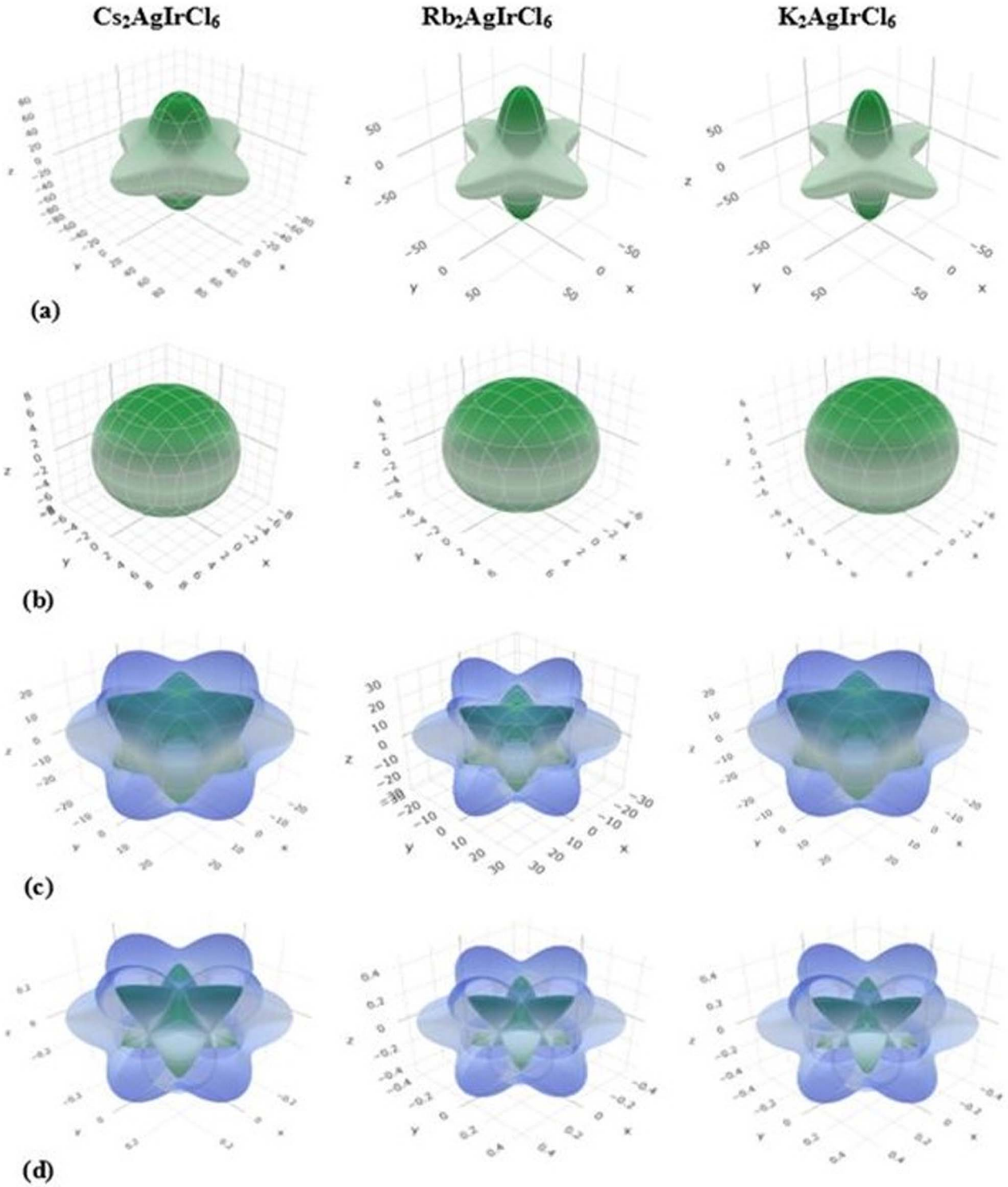

Fig. 9 Three-dimensional directional profiles of (a) Young's modulus, (b) linear compressibility, (c) shear modulus, and (d) Poisson's ratio for the $Cs_2AgIrCl_6$, $Rb_2AgIrCl_6$, and $K_2AgIrCl_6$ compounds.

In the equation mentioned, $\hbar$ denotes the normalized Planck's constant, k_B signifies Boltzmann's constant, n stands for the number of atoms, V indicates the volume, and v_m refers to the average velocity of sound. Additionally, v_m can be determined using the following formula:[108]

$$v_m = \frac{1}{3}\left[\frac{2}{v_t^3} + \frac{1}{v_l^3}\right]^{-1/3} \quad (19)$$

Table 7 Calculated density (ρ), sound velocities—longitudinal (v_l), transverse (v_t), and average (v_m) along with Debye temperature (θ_D) and melting temperature (T_m) for $A_2AgIrCl_6$ compounds where A = Cs, Rb, K

Parameters	$Cs_2AgIrCl_6$	$Rb_2AgIrCl_6$	$K_2AgIrCl_6$
$\rho \times 10^3$(Kg m^{-3})	4.89	4.42	3.89
v_l (m s^{-1})	3930.01	4164.74	4327.21
v_t (m s^{-1})	2217.58	2277.51	2328.53
v_m (m s^{-1})	2466.74	2539.68	2599.67
θ_D (K)	246.24	256.63	263.82
T_m (K)	1089.97	1142.31	1130.65

In the above expression, v_t represents the transverse sound velocity, while v_l denotes the longitudinal sound velocity. Both v_t and v_l can be computed using the given equation:[108]

$$v_t = \left[\frac{G}{\rho}\right]^{1/2} \quad (20)$$

$$v_l = \left[\frac{3B + 4G}{3\rho}\right]^{1/2} \quad (21)$$

The Debye temperatures have been found to be 246.24 K, 256.63 K, and 263.82 K for $Cs_2AgIrCl_6$, $Rb_2AgIrCl_6$, and $K_2AgIrCl_6$, respectively.

Materials used in the manufacturing of solar cells are heated to high temperatures for procedures like the formation of metal contact or the development of crystalline silicon. A material with a low melting point runs the danger of deforming, cracking, or even melting in these circumstances, creating flaws that impair the finished product's functionality. However, if the melting point of the material is too high, the fabrication process becomes more difficult and costly. Since it offers a helpful indicator of the material's resistance to deformation under heat, the elastic constant C_{11} is frequently employed to calculate a material's melting temperature. The following formula can be used to determine the melting temperature:[109]

$$T_m = (553 + 5.91C_{11})K \quad (22)$$

The estimated melting temperatures indicate that these compounds can be synthesized under ambient conditions. Of the three, $Rb_2AgIrCl_6$ has a higher melting temperature than both $Cs_2AgIrCl_6$ and $K_2AgIrCl_6$. The thermodynamic properties calculated from the elastic constants are listed in Table 7.

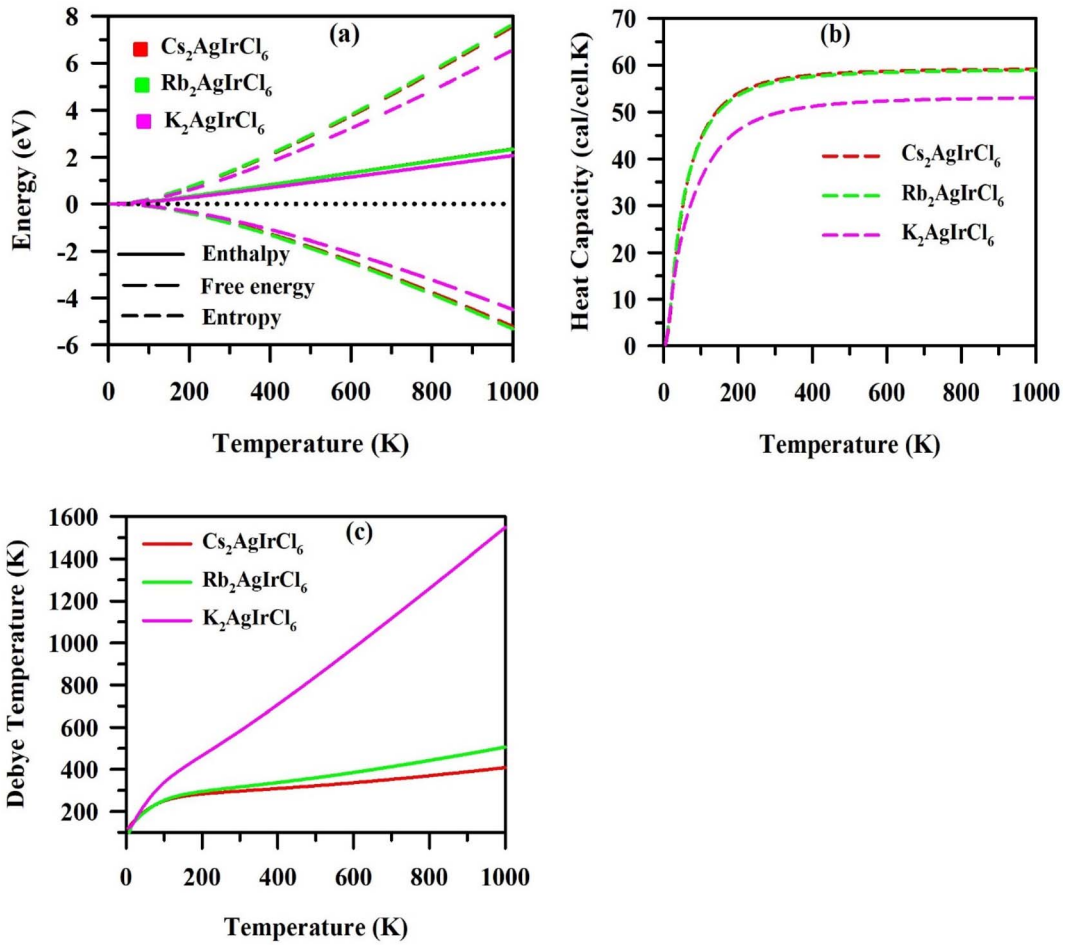

Fig. 10 (a–c)Thermodynamical properties of $A_2AgIrCl_6$ compounds where A = Cs, Rb, K.

We assessed the stability of the sample by analyzing its phonon modes at various temperatures, which allowed us to calculate key thermodynamic values like enthalpy, free energy, and entropy. These values are influenced by the frequency of phonon vibrations, which are derived by:[110]

$$H(T) = E_{\text{tot}} + \frac{1}{2}\int g(\omega)\hbar\omega \mathrm{d}\omega + \int \frac{\hbar\omega}{e^{\frac{\hbar\omega}{K_B T}} - 1} g(\omega)\mathrm{d}\omega \quad (23)$$

$$F(T) = E_{\text{tot}} + \frac{1}{2}\int g(\omega)\hbar\omega \mathrm{d}\omega + K_B T \int g(\omega)\ \ln\left(1 - e^{\frac{\hbar\omega}{K_B T}}\right)\mathrm{d}\omega \quad (24)$$

$$S(T) = K_B\left[\int \frac{\frac{\hbar\omega}{K_B T}}{e^{\frac{\hbar\omega}{K_B T}} - 1} g(\omega)\mathrm{d}\omega - \int g(\omega)\ \ln\left(1 - e^{\frac{\hbar\omega}{K_B T}}\right)\mathrm{d}\omega\right] \quad (25)$$

In this context, $g(\omega)$ represents the phonon density of states, k_B stands for the Boltzmann's constant, E_{tot} denotes the minimum total energy, and $\hbar$ refers to the reduced Planck constant. Fig. 10 shows how the predicted thermodynamic parameters of the $A_2AgIrCl_6$ compounds with temperature owing to phonon states. These variables include enthalpy, free energy, entropy, heat capacity, and Debye temperature. The data shows that while free energy falls with temperature, enthalpy, entropy, and heat capacity all rise.

Additionally, we note a more significant enhancement in the heat capacity of the $A_2AgIrCl_6$ compounds compared to changes in enthalpy and entropy, suggesting its heightened sensitivity to temperature variations. According to the data in Fig. 10a, the enthalpy, entropy, and free energy values at room temperature are determined as 0.56 (0.56, 0.47) eV, 1.33 (1.36, 1.13) eV, and 0.77 (0.80, 0.66) eV, respectively, for $Cs_2AgIrCl_6$ ($Rb_2AgIrCl_6$, $K_2AgIrCl_6$). The computed enthalpy values at 1000 K are 2.35 eV, 2.34 eV, and 2.07 eV for $Cs_2AgIrCl_6$, $Rb_2AgIrCl_6$, and $K_2AgIrCl_6$, respectively. The heat capacity gradually rises with temperature and eventually stabilizes at 59.45 (58.85, 53.03) cal/cell.K for $Cs_2AgIrCl_6$ ($Rb_2AgIrCl_6$, $K_2AgIrCl_6$) shown in Fig. 10b, a phenomenon known as the Dulong-Petit limit.[111] The variation of Debye temperature as a function of temperature is shown in Fig. 10c. For the compounds $Cs_2AgIrCl_6$, $Rb_2AgIrCl_6$, and $K_2AgIrCl_6$, the estimated Debye temperature at 0 K is about 116.96 K, 85.87 K, and 122.04 K, respectively. Under constant pressure, the Debye temperature rises with temperature. These thermodynamic characteristics provide insights for comparing with experimental results to predict phase stability.

4 Conclusions

This study systematically addresses three new $A_2AgIrCl_6$ compounds (A = Cs, Rb, K) and analyzes their structural, electrical, optical, mechanical, and thermophysical characteristics using first-principles calculations. Stability analyses suggest that these compounds are structurally, thermodynamically, and dynamically stable within the present theoretical framework. The computed electronic structures indicate that the direct band gap of $Cs_2AgIrCl_6$, $Rb_2AgIrCl_6$, and $K_2AgIrCl_6$ are 1.43 eV, 1.50 eV, and 1.55 eV, respectively, which fall within a favorable range for optoelectronic applications. The relatively low value of electron effective masses and exciton binding energies suggest beneficial charge transport and separation characteristics. In addition, the study of the optical properties indicates strong visible light absorption characteristics (up to 10^5 cm^{-1}) and very low reflectivity, which suggests their promise for use as light-harvesting materials. Mechanical parameters such as Pugh's ratio, Cauchy pressure, and Poisson's ratio indicate ductile and anisotropic characteristics, reflecting structural robustness. The calculated mechanical and thermophysical descriptors suggest potentially favorable stability within the limits of the present theoretical approach. Among the investigated compounds, $K_2AgIrCl_6$ appears comparatively less robust than the Cs- and Rb-based analogues based on the calculated stability-related parameters. Collectively, this study provides theoretical evidence that $A_2AgIrCl_6$ compounds are promising lead-free double perovskites with favorable optoelectronic characteristics. These findings offer useful guidance for future experimental studies and device-oriented investigations.

Ethical statement

This work did not require ethical approval from a human subject or animal welfare committee.

Author contributions

M. A. Rayhan: writing – original draft, methodology, conceptualization, formal analysis, data calculations, validation. M.M. Hossain: writing – review & editing, validation. M.M. Uddin: writing – review & editing, validation. M.A. Ali: conceptualization, formal analysis, validation, writing – review & editing, supervision, software.

Conflicts of interest

We declare that we have no competing interests.

Data availability

Data used in this study are available from the corresponding author upon appropriate request.

Supplementary information (SI) is available. See DOI: https://doi.org/10.1039/d6ra02981g.

Acknowledgements

This work was carried out with the aid of a grant (grant number: 21-378 RG/PHYS/AS_G -FR3240319526) from UNESCO-TWAS and the Swedish International Development Co-operation Agency (SIDA). The views expressed herein do not necessarily represent those of UNESCO-TWAS, SIDA or its Board of Governors.

References

1 L. Schlapbach and A. Borgschulte, *Hydrogen as a Future Energy Carrier*, Wiley-VCH, 2008.
2 J. R. Petit, J. Jouzel, D. Raynaud, N. I. Barkov, J. M. Barnola, I. Basile, M. Bender, J. Chappellaz, M. Davis, G. Delaygue and M. Delmotte, *Nature*, 1999, **399**, 429–436.
3 P. M. Vignais and B. Billoud, *Chem. Rev.*, 2007, **107**, 4206–4272.
4 V. Artero and M. Fontecave, *Coord. Chem. Rev.*, 2005, **249**, 1518–1535.
5 J. F. Capon, F. Gloaguen, P. Schollhammer and J. Talarmin, *Coord. Chem. Rev.*, 2005, **249**, 1664–1676.
6 M. C. Weidman, A. J. Goodman and W. A. Tisdale, *Chem. Mater.*, 2017, **29**, 5019–5030.
7 M. Liu, M. B. Johnston and H. J. Snaith, *Nature*, 2013, **501**, 395–398.
8 J. Burschka, N. Pellet, S. J. Moon, R. Humphry-Baker, P. Gao, M. K. Nazeeruddin and M. Gratzel, *Nature*, 2013, **499**, 316–319.
9 T. M. Brenner, D. A. Egger, L. Kronik, G. Hodes and D. Cahen, *Nat. Rev. Mater.*, 2016, **1**, 1–16.
10 F. Giustino and H. J. Snaith, *ACS Energy Lett.*, 2016, **1**, 1233–1240.
11 M. R. Filip, S. Hillman, A. A. Haghighirad, H. J. Snaith and F. Giustino, *J. Phys. Chem. Lett.*, 2016, **7**, 2579–2585.
12 E. T. McClure, M. R. Ball, W. Windl and P. M. Woodward, *Chem. Mater.*, 2016, **28**, 1348–1354.
13 A. H. Slavney, T. Hu, A. M. Lindenberg and H. I. A. Karunadasa, *J. Am. Chem. Soc.*, 2016, **138**, 2138–2141.
14 G. Volonakis, M. R. Filip, A. A. Haghighirad, N. Sakai, B. Wenger, H. J. Snaith and F. Giustino, *J. Phys. Chem. Lett.*, 2016, **7**, 1254–1259.
15 K. Mkadra-Gackowska, M. Gackowski and L. Szeleszczuk, *Phys. B:Condens. Matter*, 2026, **726**, 418286.
16 P. Zhang, J. Yang and S. H. Wei, *J. Mater. Chem. A*, 2018, **6**, 1809–1815.
17 X. G. Zhao, J. H. Yang, Y. Fu, D. Yang, Q. Xu, L. Yu and S. H. Wei, *J. Am. Chem. Soc.*, 2017, **139**, 2630–2638.
18 Z. Xiao, K. Z. Du, W. Meng, J. Wang, D. B. Mitzi and Y. Yan, *J. Am. Chem. Soc.*, 2017, **139**, 6054–6057.
19 S. Mahmud, M. A. Ali, M. M. Hossain and M. M. Uddin, *Vacuum*, 2024, **221**, 112926.
20 M. Saeed, I. U. Haq, A. S. Saleemi, S. U. Rehman, B. U. Haq, A. R. Chaudhry and I. Khan, *J. Phys. Chem. Solids*, 2022, **160**, 110302.
21 P. R. Varadwaj, *Nanomaterials*, 2020, **10**, 973.
22 K. Radja, B. L. Farah, A. Ibrahim, D. Lamia, I. Fatima, B. Nabil, A. Mohamed, Y. Al-Douri and A. F. Abd El-Rehim, *J. Phys. Chem. Solids*, 2022, **167**, 110795.
23 X. Cao, L. Kang, S. Guo, M. Zhang, Z. Lin and J. Gao, *ACS Appl. Mater. Interfaces*, 2019, **11**, 38648–38653.
24 Y. Xian, H. Yin, Y. Bao, Y. Xiao, S. Yuan, N. U. Rahman, Y. Yuan, Y. Zhang, X. Meng, S. Jin and W. Li, *J. Phys. Chem. Lett.*, 2020, **11**, 9535–9542.
25 H. Yin, Y. Xian, Y. Zhang, W. Chen, X. Wen, N. U. Rahman, Y. Long, B. Jia, J. Fan and W. Li, *Adv. Funct. Mater.*, 2020, **30**, 2002225.
26 X. Wang, X. Zhang, S. Yan, H. Liu and Y. Zhang, *Angew. Chem., Int. Ed.*, 2022, **61**, e202210853.
27 L. Chávez-Guerrero, B. Medina-Lott, R. F. Cienfuegos, M. A. Garza-Navarro, R. N. Vannier, A. Ringuede, M. Hinojosa and M. Cassir, *J. Rare Earths*, 2015, **33**, 277–281.
28 B. Yan, A. K. Paul, S. Kanungo, M. Reehuis, A. Hoser, D. M. Tobbens, W. Schnelle, R. C. Williams, T. Lancaster, F. Xiao and J. S. Moller, *Phys. Rev. Lett.*, 2014, **112**, 147202.
29 M. Zeppieri, P. L. Villa, N. Verdone, M. Scarsella and P. De Filippis, *Appl. Catal., A*, 2010, **387**, 147–154.
30 L. Bufaiçal, M. A. Heringer, J. R. Jesus, A. Caytuero, C. Macchiutti, E. M. Bittar and E. Baggio-Saitovitch, *J. Magn. Magn. Mater.*, 2022, **556**, 169408.
31 M. U. Din, J. Munir, M. Jamil, M. A. Saeed and Q. Ain, *Phys. B:Condens. Matter*, 2022, **627**, 413533.
32 P. R. Varadwaj and H. M. Marques, *J. Mater. Chem. C*, 2020, **8**, 12968–12983.
33 P. R. Varadwaj and H. M. Marques, *Front. Chem.*, 2020, **8**, 796.
34 M. Caid, Y. Rached, D. Rached and H. Rached, *J. Mol. Model.*, 2023, **29**, 178.
35 L. Szeleszczuk, K. Mkadra-Gackowska, V. B. Hacholli and M. Gackowski, *J. Phys. Chem. Solids*, 2025, **209**, 113293.
36 H. H. Hegazy, G. M. Mustafa, A. Nawaz, N. A. Noor, A. Dahshan and I. Boukhris, *J. Mater. Res. Technol.*, 2022, **19**, 1271–1281.
37 V. Deswal, S. Kaushik, R. Kundara and S. Baghel, *Mater. Sci. Eng. B*, 2024, **299**, 117041.
38 M. S. Parves, M. A. Siddique, M. Tarekuzzaman, N. Shahadath, S. Ahmad, M. Rasheduzzaman, M. M. Hossen, Y. Arafat and M. Z. Hasan, *Energy Nexus*, 2025, **20**, 100549.
39 M. A. Bakkar Siddique, M. S. Parves, M. Tarekuzzaman, M. R. Kabir, M. S. Al-Saleem, J. Y. Al-Humaidi, M. Rasheduzzaman, M. M. Hossen, M. M. Rahman and M. Z. Hasan, *Langmuir*, 2025, **41**, 19797–19820.
40 L. Szeleszczuk, K. Mkadra-Gackowska and M. Gackowski, *Phys. B:Condens. Matter*, 2025, **719**, 417958.
41 P. Hohenberg and W. Kohn, *Phys. Rev.*, 1964, **136**, B864.
42 W. Kohn and L. J. Sham, *Phys. Rev.*, 1965, **140**, A1133.
43 P. Blaha, K. Schwarz, P. Sorantin and S. B. Trickey, *Comput. Phys. Commun.*, 1990, **59**, 399–415.
44 K. Schwarz, P. Blaha and G. K. H. Madsen, *Comput. Phys. Commun.*, 2002, **147**, 71–76.
45 J. P. Perdew, K. Burke and M. Ernzerhof, *Phys. Rev. Lett.*, 1996, **77**, 3865.
46 F. D. Murnaghan, *Proc. Natl. Acad. Sci. U. S. A.*, 1944, **30**, 244–247.
47 F. Tran and P. Blaha, *Phys. Rev. Lett.*, 2009, **102**, 226401.
48 K. Momma and F. Izumi, *J. Appl. Crystallogr.*, 2011, **44**, 1272–1276.

49 M. D. Segall, P. J. Lindan, M. A. Probert, C. J. Pickard, P. J. Hasnip, S. J. Clark and M. C. Payne, *J. Phys. Condens. Matter*, 2002, **14**, 2717–2744.
50 K. Lv, S. Qi, G. Liu, Y. Lou, J. Chen and Y. Zhao, *Chem. Commun.*, 2019, **55**, 14741–14744.
51 Z. Li, F. Sun, H. Song, H. Zhou, Z. Yuan, P. Guo, G. Zhou, Q. Zhuang and X. Yu, *Dalton Trans.*, 2021, **50**, 9804–9811.
52 M. A. Hadi, M. N. Islam and J. Podder, *RSC Adv.*, 2022, **12**, 15461–15469.
53 X. Du, D. He, H. Mei, Y. Zhong and N. Cheng, *Phys. Lett. A*, 2020, **384**, 126169.
54 V. M. Goldschmidt, *Naturwissenschaften*, 1926, **14**, 477–485.
55 C. Li, X. Lu, W. Ding, L. Feng, Y. Gao and Z. Guo, *Acta Crystallogr., Sect. B: Struct. Sci.*, 2008, **64**, 702–707.
56 C. J. Bartel, C. Sutton, B. R. Goldmith, R. Ouyang, C. B. Musgrave, L. M. Ghiringhelli and M. Scheffler, *Sci. Adv.*, 2019, **5**, eaav0693.
57 R. D. Shannon, *Acta Crystallogr., Sect. A*, 1976, **32**, 751–767.
58 M. Archi, O. Bajjou and B. Elhadadi, *Int. J. Hydrogen Energy*, 2025, **105**, 759–770.
59 M. Jawad, A. U. Rahman, S. H. Mirza, N. ul Amin, M. Faizan, A. S. Alsubaie and S. M. El-Bahy, *Chem. Phys.*, 2025, **588**, 112463.
60 M. H. Mia, M. Y. H. Khan, M. Rasheduzzaman and M. Z. Hasan, *Mater. Des.*, 2026, **263**, 115665.
61 A. Nadeem, A. I. Bashir, S. Azam, A. U. Rahman and M. A. Iqbal, *Eur. Phys. J. Plus*, 2023, **138**, 328.
62 M. A. Ali and A. K. M. A. Islam, *Phys. B:Condens. Matter*, 2012, **407**, 1020–1026.
63 M. A. Ali, M. Roknuzzaman, M. T. Nasir, A. K. M. A. Islam and S. H. Naqib, *Int. J. Mod. Phys. B*, 2016, **30**, 1650089.
64 M. R. Islam, A. Zahid, M. A. Rahman, M. F. Rahman, M. A. Islam, M. K. Hossain, M. A. Ali, M. A. Iqbal, F. I. Bakhsh and S. Ahmad, *J. Phys. Chem. Solids*, 2024, **184**, 111722.
65 F. Tran and P. Blaha, *Phys. Rev. Lett.*, 2009, **102**, 226401.
66 H. Jiang, *J. Chem. Phys.*, 2013, **138**, 134115.
67 P. Borlido, J. Schmidt, A. W. Huran, F. Tran, M. A. Marques and S. Botti, *npj Comput. Mater.*, 2020, **6**, 96.
68 M. Y. Sofi, M. S. Khan, J. Ali and M. A. Khan, *Sci. Rep.*, 2024, **14**, 5520.
69 T. Nakajima and K. Sawada, *J. Phys. Chem. Lett.*, 2017, **8**, 4826–4831.
70 H. C. Wang, P. Pistor, M. A. L. Marques and S. Botti, *J. Mater. Chem. A*, 2019, **7**, 14705–14711.
71 Y. Tang, J. Zhang, X. Zhong, Q. Wang, H. Zhang, C. Ren and J. Wang, *Sol. Energy*, 2019, **190**, 272–277.
72 G. Volonakis, A. A. Haghighirad, R. L. Milot, W. H. Sio, M. R. Filip, B. Wenger, M. B. Johnston, L. M. Herz, H. J. Snaith and F. Giustino, *J. Phys. Chem. Lett.*, 2017, **8**, 772–778.
73 C. Kittel and P. McEuen, *Introduction to Solid State Physics*, John Wiley & Sons, 2018.
74 P. Umari, E. Mosconi and F. De Angelis, *Sci. Rep.*, 2014, **4**, 4467.
75 L. K. Gao and Y. L. Tang, *ACS Omega*, 2021, **6**, 11545–11555.
76 G. C. La Rocca, *Thin Films Nanostruct.*, 2003, **31**, 97–128.
77 S. Mahmud, U. Ahmed, M. A. Atik, M. M. Hossain, M. M. Uddin and M. A. Ali, *Phys. Chem. Chem. Phys.*, 2025, **27**, 4686–4703.
78 C. J. Yu, I. C. Ri, H. M. Ri, J. H. Jang, Y. S. Kim and U. G. Jong, *RSC Adv.*, 2023, **13**, 16012–16022.
79 M. A. Rayhan, M. M. Hossain, M. M. Uddin and M. A. Ali, *RSC Adv.*, 2026, **16**, 16442–16459.
80 R. Hoffmann, *Rev. Mod. Phys.*, 1988, **60**, 601.
81 C. D. Gelatt Jr, A. R. Williams and V. L. Moruzzi, *Phys. Rev. B*, 1983, **27**, 2005.
82 S. Mahmud, M. M. Hossain, M. M. Uddin and M. A. Ali, *J. Phys. Chem. Solids*, 2025, **196**, 112298.
83 M. Wuttig, C. F. Schon, M. Schumacher, J. Robertson, P. Golub, E. Bousquet, C. Gatti and J. Y. Raty, *Adv. Funct. Mater.*, 2022, **32**, 2110166.
84 G. Murtaza and I. Ahmad, *Phys. B:Condens. Matter*, 2011, **406**, 3222–3229.
85 L. K. Gautam, H. Haneef, M. M. Junda, D. B. Saint John and N. J. Podraza, *Thin Solid Films*, 2014, **571**, 548–553.
86 S. A. Dar and B. Want, *Solid State Commun.*, 2022, **355**, 114928.
87 D. Gill, P. Bhumla, M. Kumar and S. Bhattacharya, *J. Phys. Mater.*, 2021, **4**, 25005.
88 R. D. Grimes and E. R. Cowley, *Can. J. Phys.*, 1975, **53**, 2549–2554.
89 V. S. Zhandun and V. I. Zinenko, *J. Alloys Compd.*, 2016, **671**, 184–191.
90 Z. Jin, Y. Wu, S. Li, Q. Wu, S. Chen, Y. Chen, W. Zhang and C. Zhang, *Results Phys.*, 2021, **22**, 103860.
91 E. F. Schubert, J. K. Kim and J. Q. Xi, *Phys. Status Solidi*, 2007, **244**, 3002–3008.
92 G. V. G. Baranoski and A. Krishnaswamy, *Light and Skin Interactions: Simulations for Computer Graphics Applications*, Morgan Kaufmann, 2010.
93 R. Yang, D. Li, S. L. Salazar, Z. Rao, M. Arici and W. Wei, *Sol. Energy Mater. Sol. Cells*, 2021, **219**, 110792.
94 Q. Wang, Z. Hu and X. Shao, *AIP Adv.*, 2020, **10**, 045010.
95 T. Y. Tang and Y. L. Tang, *Chem. Phys.*, 2023, **570**, 111897.
96 D. Y. Hu, X. H. Zhao, T. Y. Tang, L. M. Lu, L. Li, L. K. Gao and Y. L. Tang, *Mater. Today Commun.*, 2021, **29**, 102842.
97 M. A. Rehman, J. ur Rehman and M. B. Tahir, *J. Phys. Chem. Solids*, 2023, **181**, 111443.
98 J. Tauc and A. Menth, *J. Non-Cryst. Solids*, 1972, **8**, 569–585.
99 P. Makuła and W. Pacia Michałand Macyk, *J. Phys. Chem. Lett.*, 2018, **9**, 6814–6817.
100 X. Q. Chen, H. Niu, D. Li and Y. Li, *Intermetallics*, 2011, **19**, 1275–1281.
101 X. Wang, H. Xiang, X. Sun, J. Liu, F. Hou and Y. Zhou, *J. Mater. Sci. Technol.*, 2015, **31**, 369–374.
102 D. C. Wallace and H. Callen, *Am. J. Phys.*, 1972, **40**, 1718–1719.
103 R. Hill, *Proc. Phys. Soc., Sect. A*, 1952, **65**, 349.
104 M. A. Hadi, *J. Phys. Chem. Solids*, 2020, **138**, 109275.
105 S. F. Pugh, *Philos. Mag. J. Sci.*, 1954, **45**, 823–843.
106 S. I. Ranganathan and M. Ostoja-Starzewski, *Phys. Rev. Lett.*, 2008, **101**, 55504.

107 R. Gaillac, P. Pullumbi and F. Coudert, *J. Phys. Condens. Matter*, 2016, **28**, 275201.
108 K. D. Jayan and V. Sebastian, *Mater. Today Commun.*, 2021, **28**, 102650.
109 S. A. Dar, V. Srivastava and U. K. Sakalle, *Mater. Res. Express*, 2017, **4**, 86304.
110 S. Baroni, S. De Gironcoli, A. Dal Corso and P. Giannozzi, *Rev. Mod. Phys.*, 2001, **73**, 515.
111 D. Wu, S. Huang, D. Feng, B. Li, Y. Chen, J. Zhang and J. He, *Phys. Chem. Chem. Phys.*, 2016, **18**, 23872–23878.